Available online at www.sciencedirect.com
ScienceDirect
Journal of Nuclear Materials 371 (2007) 176–201
journal of nuclear materials
www.elsevier.com/locate/jnucmat

# Corrosion and stress corrosion cracking in supercritical water

G.S. Was [a,*], P. Ampornrat [a], G. Gupta [a], S. Teysseyre [a], E.A. West [a], T.R. Allen [b], K. Sridharan [b], L. Tan [b], Y. Chen [b], X. Ren [b], C. Pister [b]

[a] University of Michigan, Nuclear Engineering, 1911 Cooley, Ann Arbor, MI 48109, United States
[b] University of Wisconsin, United States

**Abstract**

Supercritical water (SCW) has attracted increasing attention since SCW boiler power plants were implemented to increase the efficiency of fossil-based power plants. The SCW reactor (SCWR) design has been selected as one of the Generation IV reactor concepts because of its higher thermal efficiency and plant simplification as compared to current light water reactors (LWRs). Reactor operating conditions call for a core coolant temperature between 280 °C and 620 °C at a pressure of 25 MPa and maximum expected neutron damage levels to any replaceable or permanent core component of 15 dpa (thermal reactor design) and 100 dpa (fast reactor design). Irradiation-induced changes in microstructure (swelling, radiation-induced segregation (RIS), hardening, phase stability) and mechanical properties (strength, thermal and irradiation-induced creep, fatigue) are also major concerns. Throughout the core, corrosion, stress corrosion cracking, and the effect of irradiation on these degradation modes are critical issues. This paper reviews the current understanding of the response of candidate materials for SCWR systems, focusing on the corrosion and stress corrosion cracking response, and highlights the design trade-offs associated with certain alloy systems. Ferritic–martensitic steels generally have the best resistance to stress corrosion cracking, but suffer from the worst oxidation. Austenitic stainless steels and Ni-base alloys have better oxidation resistance but are more susceptible to stress corrosion cracking. The promise of grain boundary engineering and surface modification in addressing corrosion and stress corrosion cracking performance is discussed.


## 1. Introduction

One of the most promising advanced reactor concepts for Generation IV nuclear reactors is the Supercritical Water Reactor (SCWR). Operating above the thermodynamic critical point of water (374 °C, 22.1 MPa), the SCWR offers many advantages compared to state-of-the-art LWRs including the use of a single phase coolant with high enthalpy, the elimination of components such as steam generators and steam separators and dryers, a low coolant mass inventory resulting in smaller components, and a much higher efficiency (~45% vs. 33% in current LWRs). Overall, the design provides a simplified, reduced volume system with high thermal efficiency. The challenge is provided by the substantial increase in operating temperature and pressure as compared to current BWR and PWR designs. The reference design for the SCWR [1,2] calls for an operating pressure of 25 MPa and an outlet water temperature up to 620 °C, Fig. 1.

Since supercritical water has never been used in nuclear power applications, there are numerous

* Corresponding author. Fax: +1 734 763 4540.
*E-mail address:* gsw@engin.umich.edu (G.S. Was).

0022-3115/$ - see front matter © 2007 Elsevier B.V. All rights reserved.
doi:10.1016/j.jnucmat.2007.05.017

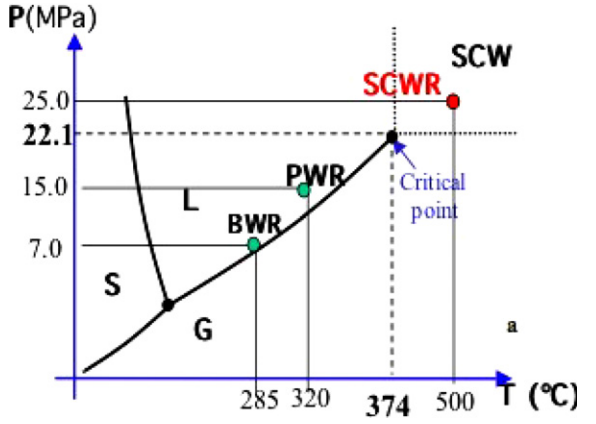


Fig. 1. Pressure–temperature regime of SCWR operation compared to that for current BWRs and PWRs.

potential problems, particularly with materials. Water in the supercritical phase exhibits properties significantly different from those of liquid water below the critical point. It acts like a dense gas and its density can vary with temperature and pressure from less than 0.1 g/cc to values similar to that of water below the critical point. This allows one to 'tune' the properties of SCW, such as the ion product, heat capacity, and dielectric constant, to fit the application of interest [1]. The corrosive behavior of SCW over this range of densities varies widely depending upon the values of these properties [3,4].

Supercritical water will, at the high reactor outlet temperatures, fall in the lower end of the density scale at around 0.2 g/cc while having higher density at the reactor inlet. At the low density associated with the reactor outlet, water is a non-polar solvent and can dissolve gases like oxygen to complete miscibility. Depending upon what species are present and how much oxygen is present in the solution, SCW in this state can become a very aggressive oxidizing environment [3,5]. On the other hand, the solubility of ionic species is expected to be extremely low. This is a cause for concern for the general corrosion and stress corrosion cracking (SCC) susceptibility of the structural materials and fuel elements of reactors.

While no experience exists with supercritical water reactors there is a significant operating history with supercritical fossil plants [6,7]. In fact, as of 2004, there were some 268 944 MWe (462 units) of installed capacity of coal-fired supercritical water power plants worldwide [7]. Hence there is significant industry experience with supercritical water in power generation. However, a nuclear reactor core is significantly different from a fossil-fired boiler. One key difference is geometry. A fossil-fired boiler consists of a large number of fire tubes that circulate water on the inside. These tubes have relatively thick walls, approximately 6–12 mm in thickness. Further, the water sees a geometrically smooth and simple surface along its path through the boiler. Contrast this with the core of an SCWR, which consists of fuel rods, control rods, and water rods comprising a fuel assembly with some 145 assemblies forming the core. The wall thickness for the fuel rod cladding in the reference SCWR design is 0.63 mm and the wall thickness for the water rods is 0.40 mm. These very thin components do not provide much margin for corrosion in the cores of supercritical water reactors. Oxide films of several hundred micrometer thickness are not unusual for boiler tubes with typical wall thicknesses in the 6–12 mm range, but are unacceptable for water rods or fuel cladding. Fig. 2 illustrates the scale differences between core components in an SCWR and the corresponding components in a fossil-fired SCW power plant.

Reactor core components must also contend with irradiation that can affect both the water chemistry and the alloy microstructure. Radiolysis can result in an increase in the concentration of oxygen and other oxidizing species such as $H_2O_2$ that raise the corrosion potential and increase susceptibility to processes such as stress corrosion cracking. Radiolysis is not at all understood in supercritical water and pioneering experiments are just now underway. The very high-temperatures and significantly different properties of SCW compared to subcritical water make it difficult to estimate the effect of irradiation on this fluid. Initial measurements have shown that virtually no free radical reaction rates follow an Arrhenius law, and so the rate constants must be measured [8]. Bartels et al. [8] have made measurements on the radiolysis yield of $H_2$ as a function of temperature and have found that it increases steeply with temperature above about 350 °C, Fig. 3a. They have also found that rate constants for the reactions $H_2 + OH$ (Fig. 3b) and $OH + OH$ decrease at higher temperature indicating a slow down of the reaction rate at high-temperature. Since hydrogen addition is a key strategy in controlling corrosion at high-temperature in current reactor designs, an understanding of the dependence of this reaction (Fig. 3b) on temperature and radiation may be critical to controlling the corrosion potential in the core of an SCWR. A measure of

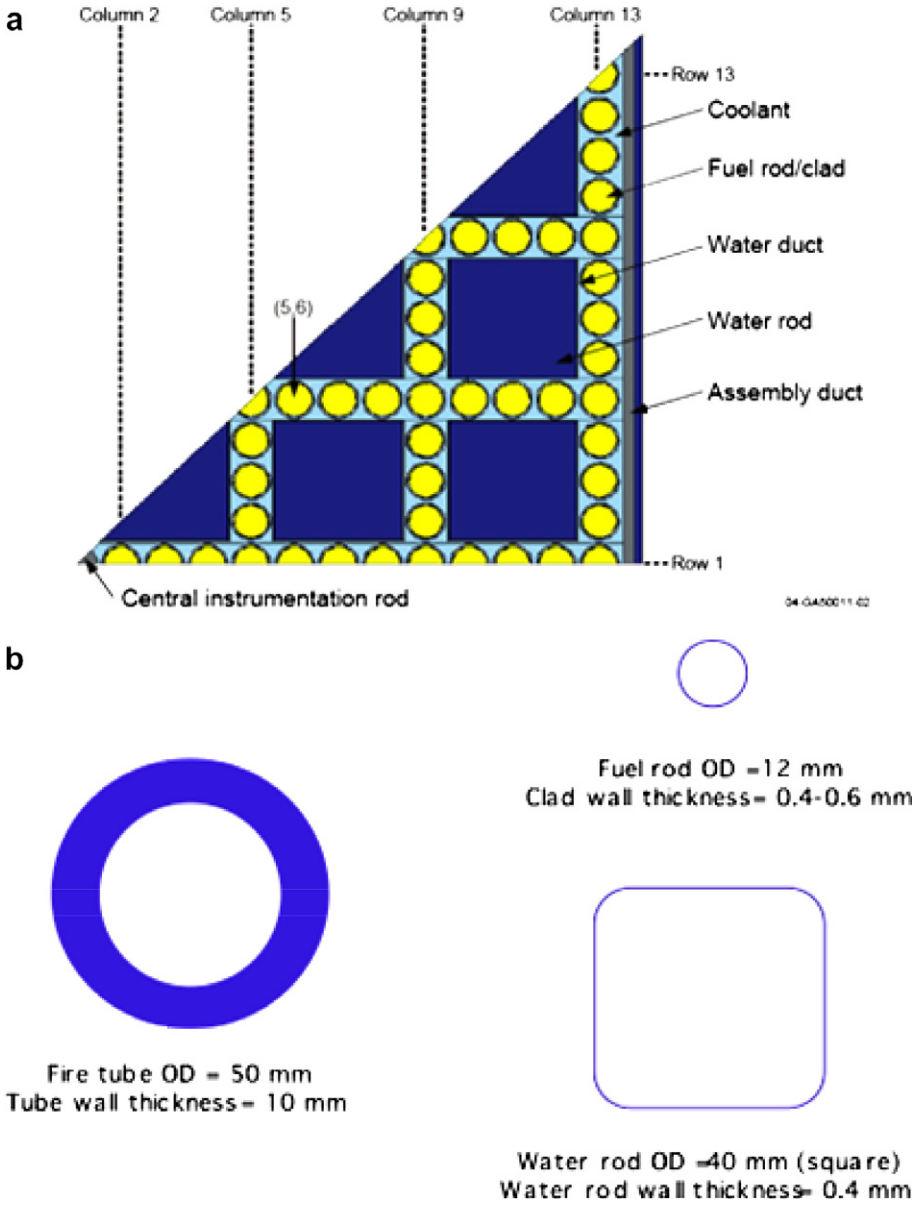


Fig. 2. (a) A 1/8 assembly model of the 21 × 21 SCWR fuel assembly [2], and (b) comparison of typical fossil boiler tube dimensions to fuel rod and water rod dimensions in the reference SCWR design.

the corrosion potential in supercritical water will require development of a reference electrode that can withstand the SCW environment. Once the irradiated water chemistry is understood so that the corrosion potential can be estimated or measured, then laboratory experiments can be carried out to more accurately simulate the environmental conditions expected for the core of a SCWR.

Perhaps the most challenging problem is the role of irradiation on the microstructure and how these changes affect stress corrosion cracking. Irradiation assisted stress corrosion cracking has been a generic problem in light water reactors of all types and covering many austenitic and nickel-base alloys [9,10].

This paper reviews the current understanding of the response of candidate materials for SCWR systems, focusing on the corrosion and stress corrosion cracking response, and highlights the design trade-offs associated with certain alloy systems. With the

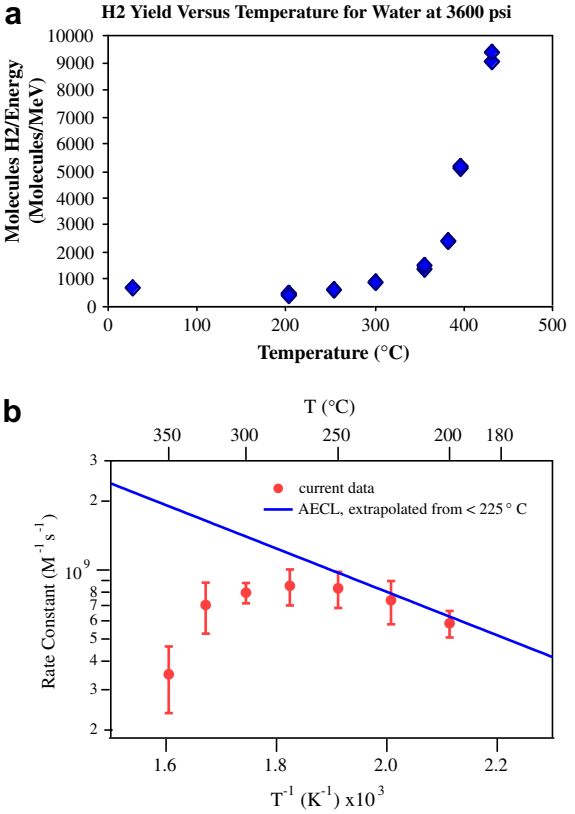


Fig. 3. (a) Hydrogen yield as a function of water temperature at 3600 psi, and (b) radiolysis yield of $H_2$ vs. temperature and rate constant for the reaction of $H_2$ with OH vs. $1/T$.

exception of the effect of irradiation on stress corrosion cracking, the important issues of radiation response and radiolysis are not addressed in this review.

## 2. Experimental programs

In support of the supercritical water reactor program, corrosion and stress corrosion cracking have been studied in pure supercritical water in ferritic-martenitic steels, austenitic stainless steels, Ni-base alloys, Zr-base alloys, and Ti-base alloys. Test temperatures have ranged from 290 to 732 °C. Dissolved oxygen concentration has ranged from <10 ppb to 8000 ppb. Exposure times for corrosion tests have ranged from 100 to over 1000 h. In stress corrosion cracking studies, the effect of chemical additions have been examined, specifically $H_2SO_4$, HCl, $H_2O_2$, NaCl. Additionally, the affect of system pressure on SCC resistance has been studied.

Some specific alloys have multiple designations. For example, HCM12A and T122 are the same composition, as are NF616 and T92. In the figures, the alloys designation used is consistent with the reference from which the data was originally published. Tables 1 and 3 can be used to determine alloys with multiple designations.

## 3. Corrosion

This section presents and summarizes the corrosion in pure supercritical water. Specific details the corrosion test procedures are described in Ref. [11]. The data and descriptions presented are distinct from that on supercritical water oxidation (SCWO) experiments that contain halides for the purpose of breaking down organic materials. This latter database will not be covered in the review that

Table 1
Summary of experiments on corrosion in pure supercritical water

| Alloy Class | Alloy | Temp. (°C) | Water chemistry | Exposure time (h) |
|---|---|---|---|---|
| Austenitic SS | 304, 304L, 316, 316L, 316 + Zr, 310, 310S, 310 + Zr, TP347H, Sanicro28, D9, 800H | 290–650 | Deaerated (<10 ppb) to 8000 ppb dissolved oxygen, | 100–1026 |
| Nickel-base | 600, 625, 690, 718, 825, C22, B2, C276, MAT21, MC | 290–600 | Deaerated (<10 ppb) to 8000 ppb dissolved oxygen, <0.1 mS/cm | 100–575 |
| Ferritic–martensitic | T91, T91a, T91b, HCM12A (T122), HCM12, HT-9 (12Cr–1Mo–1WVNb), NF616 (T92), MA956, 2.25Cr–1Mo (T11), P2 | 290–650 | Deaerated (<10 ppb) to 8000 ppb dissolved oxygen, <0.1 mS/cm | 100–1026 |
| ODS | 9Cr, 12Cr, F–M, 316, Inconel, Hastelloy G-30, 19Cr, 14Cr–4Al, 16Cr–4Al, 19Cr–4Al, 22Cr–4Al | 360–600 | 25 ppb | 200–1026 |
| Zirconium | Zr, Zr–Nb, Zr–Fe–Cr, Zr–Cr–Fe, Zr–Cu–Mo, Zr-2, Zr-4 | 400–500 | Deaerated (<10 ppb dissolved oxygen), <0.1 mS/cm | <2880 |
| Titanium | Ti–3Al–2.5V, Ti–6Al–4V, Ti–15Mo–5Zr–3Al, Ti–15V–3Al–3Sn–3Cr | 290–550 | 8000 ppb dissolved oxygen, 0.1 mS/cm | 500 |

follows. The alloy systems, specific alloys and range of test conditions is summarized in Table 1.

### 3.1. Ferritic–martensitic steels

Ferritic and martensitic (FM) steels were selected for possible use in supercritical water reactor systems because of their radiation resistance, high thermal conductivity, and low thermal expansion coefficients. To date, international programs have evaluated the following ferritic–martensitic steels: T22, P2, T91, HT9, HCM12, HCM12A (T122), NF616 (T92), and numerous oxide dispersion strengthened steels including JAEA 9Cr ODS, MA 956 and (14–22)Cr–4Al versions [11–19]. Surface modification, specifically the implantation of oxygen and yttrium, to reduce oxidation rates, has been performed on NF616 and HCM12A.

#### 3.1.1. Oxide structure

For samples exposed to low dissolved oxygen concentration (less than 300 ppb), a dual-layer oxide is formed on ferritic–martensitic steels. A typical structure and composition profile for an oxide grown on a ferritic–martensitic steel is shown in the SEM image and EDS profiles of Fig. 4. Additional information on oxide structure in ferritic–martensitic steels can be seen in Fig. 5, an EBSD image. The image and the composition profiles show two distinct layers. The oxygen content is similar in both outer and inner oxide layers. The outer oxide is predominantly iron oxide whereas the inner layer contains a significant amount of chromium. For 300 ppb and lower dissolved oxygen concentration, XRD and EBSD have revealed that the outer oxide layer is magnetite ($Fe_3O_4$) and the inner layer is an iron–chromium spinel of composition $(Fe,Cr)_3O_4$.

For samples exposed to high (2000 ppb) dissolved oxygen, an outer hematite layer also forms. The formation of a two-layer oxide in low oxygen concentration and a three-layer oxide in high oxygen concentration is consistent with predicted stable phases [20]. In addition EDS analysis of the oxygen profile shown in Fig. 4b indicates the presence of an internal oxidation transition zone underneath the inner spinel layer.

Grain morphology in each oxide layer is revealed by the EBSD map. The spinel layer is composed of small equiaxed grains with a large aspect ratio (~0.7 in average), while the magnetite layer is composed of large columnar grains with a small aspect ratio

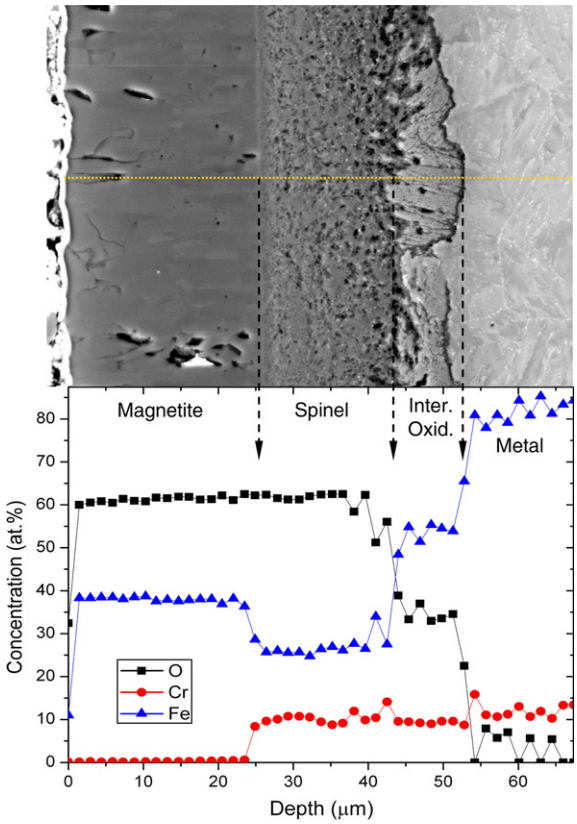


Fig. 4. Cross-section image (a) and EDS (b) of HCM12A exposed to 600 °C SCW containing 25 ppb dissolved oxygen for 1026 h. Layers are magnetite, spinel, and metal from left to right.

(~0.4 in average). The grains in the magnetite layer are elongated along the direction parallel to the growth direction of oxide scale. Carbides retained on the prior austenite grain structure in the inner oxide layer are similar to that in the ferrite phase, indicating that the oxide has grown from the ferrite by solid-state oxidation.

#### 3.1.2. Oxide kinetics

A strong correlation between increasing temperature and increased oxidation has been found for all ferritic–martensitic steels [13,15,56]. The typical effect of time and temperature on oxide growth in ferritic–martensitic steels can be seen in Figs. 6 and 7, using HCM12A as an example. At higher temperatures (500 °C and 600 °C), the growth of the oxide follows roughly parabolic kinetics (the growth exponent is ~0.4 for this small data set). At temperatures below the pseudo-critical point (371 °C), very little oxide growth is seen out to 1026 h. The oxide growth increases significantly with temperature. Activation energies have been estimated from the oxidation of

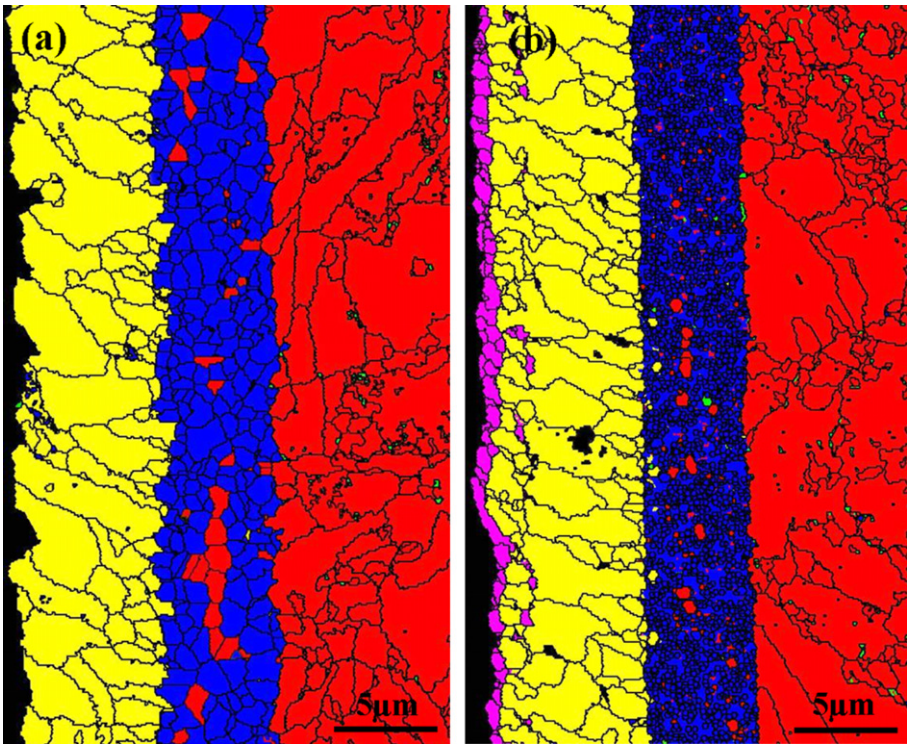


Fig. 5. Cross-section EBSD scanning maps of SCW-exposed samples (a) 500 °C, 25 ppb dissolved oxygen, 505 h and (b) 500 °C, 2000 ppb dissolved oxygen, 505 h, where base metal, spinel, magnetite, and hematite are highlighted in red, blue, yellow, and magenta, respectively. Black areas are unindexed [20]. (For interpretation of the references in colour in this figure legend, the reader is referred to the web version of this article.)

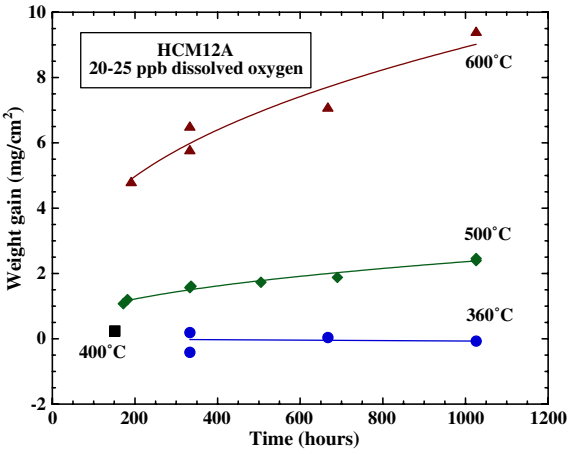


Fig. 6. Weight gain as a function of time for HCM12A exposed to low oxygen concentration supercritical water at 360 °C, 400 °C, 500 °C, and 600 °C [11].

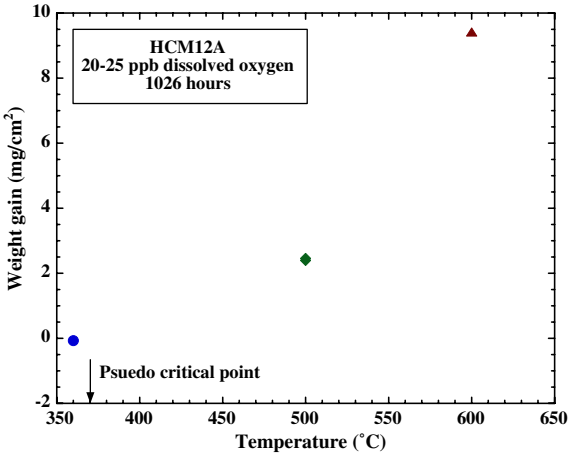


Fig. 7. Weight gain as a function of temperature for HCM12A exposed to low oxygen concentration supercritical water for 1026 h [11].

T91, HCM12A, and HT9 exposed at temperatures from 400 to 600 °C and are 189, 177, and 172 kJ/mol, respectively.

Extensive experiments by Graham and Hussey [21] have suggested that in Ni, Cr, Fe, and Fe–Cr alloys, the outer oxides grow predominantly by

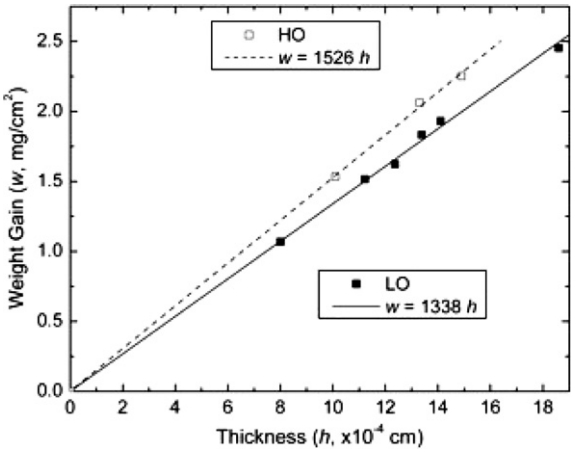


Fig. 8. Weight gain as a function of oxide thickness for HCM12A exposed to 25 ppb and 2000 ppb oxygen at 500 °C. Average oxide density (the slope of the plotted lines) is 1526 mg/cm$^2$ for 2000 ppb dissolved oxygen and 1338 mg/cm$^2$ for 25 ppb dissolved oxygen [20].

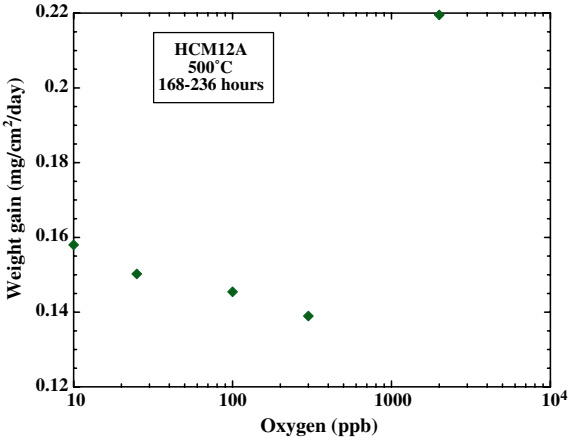


Fig. 9. Weight gain as a function of temperature for HCM12A exposed to low oxygen concentration supercritical water for 1026 h [11].

outward diffusion of cations. In particular, the activation energy for the diffusion of iron in $Fe_3O_4$ is 230 kJ/mol, for nickel in NiO the value is 234 kJ/mol, and for chromium in $Cr_2O_3$, the value is 420 kJ/mol [22]. The activation energy for diffusion of oxygen in $Fe_2O_3$ is 610 kJ/mol [21], and while that for $Fe_3O_4$ is considerably smaller, the diffusion coefficients cannot account for the measured oxide thickness. Nevertheless, evidence suggests that the inner oxide grows by the inward diffusion of oxygen. The diffusion is likely affected by short-circuit paths such as pores, cracks and grain boundaries, which would account for the higher rates.

For times to 1026 h, the oxides that develop on traditional (non-ODS versions) ferritic–martensitic steels are stable, maintain a constant average density, and do not spall. This is evident in the data presented in Fig. 8 that shows the weight gain is proportional to the oxide thickness. The oxide density is greater for samples exposed at 2000 ppb as compared to samples exposed at 25 ppb dissolved oxygen. Plan view and cross-sectional images of the dual phase oxides also do not show any indication of spallation.

### 3.1.3. Effect of dissolved oxygen

The oxide growth rate and associated weight gain of ferritic–martensitic steels are dependent on the dissolved oxygen concentration. This dependence is shown in Fig. 9 using data from HCM12A. For dissolved oxygen concentrations between 10 and 300 ppb, the weight gain associated with oxide growth decreases slightly with dissolved oxygen concentration. However, the weight gain increases significantly for samples exposed to 2000 ppb dissolved oxygen, due to the development of a thicker oxide layer. In addition, the development of a denser oxide layer and the formation of a hematite layer formed at the higher dissolved oxygen content SCW may also play a role in the upsurge in weight gain observed for samples exposed to 2000 ppb dissolved oxygen SCW.

Combined water chemistry control in fossil plants [23,24] adds small amounts of oxygen to enhance the formation of hematite crystals between the magnetite grains, thus reducing the oxidation rate, perhaps by reducing the diffusion of oxygen through the multi-phase film. For the studies supporting SCWRs, significant hematite crystals have not been found between the magnetite grains at 10–300 ppb oxygen where oxidation is the slowest.

### 3.1.4. Effect of bulk chromium concentration

For conventional ferritic–martensitic steels, increasing the bulk chromium concentration reduces the weight gain due to oxidation. An example of this correlation is shown in Fig. 10 where the 9 at.% Cr alloy NF616 has a greater weight gain than the 12 at.% alloy HCM12A. The same trend is seen in the weight gain data for T91 (9Cr) and HT9 (12Cr) for all temperatures and times evaluated. These results agree with those from Jang [15], as well as Cho and Kimura [16,25] who examined weight gain over a range of Cr content and

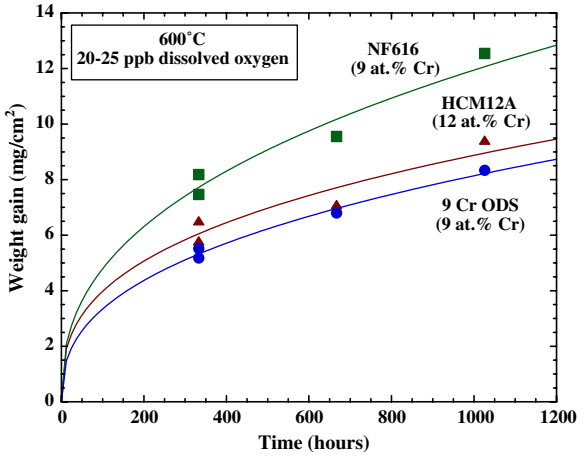


Fig. 10. Weight gain as a function of time for NF616, HCM12A, and 9Cr ODS exposed to low oxygen concentration supercritical water at 600 °C.

found that increasing Cr led to decreasing weight gain.

A different behavior is noted in oxide dispersion strengthened ferritic–martensitic steels. The weight gain data for the JAEA 9Cr ODS alloy is also included in Fig. 10. Even though this alloy only has 9 at.% Cr, it shows the lowest weight gain of any of the tested ferritic–martensitic steels. The ODS spinel that forms tends to become more porous at higher exposure times [26].

### 3.1.5. Oxidation reduction methods

As was mentioned in the introduction, the allowable oxide thickness must be limited for thin-walled cladding or water rods. For a 1026 h exposure at 600 °C, the oxide thickness in HCM12A is approximately 65 μm, approximately 15% of the thickness of the original water rod wall. For ferritic–martensitic steels to be acceptable for thin-walled components exposed to supercritical water, the thickness of the oxide (and the associated metal loss) must be reduced.

One method for improvement is seen from the ODS data in Fig. 10. The ODS steels typically show lower oxidation than conventional ferritic–martensitic steels. The ODS steels have two significant differences from conventional ferritic–martensitic steels. First, they include nanometer sized Y–Ti–O particles, added for strengthening. A comparison of the 9Cr ODS alloy with NF616, Figs. 11 and 12, shows that the ODS alloy has a much deeper internal oxidation layer. Thus the net conversion of metal to spinel appears to be driven by oxygen diffusion into the metal rather than cation diffusion to the oxide surface. Detailed microscopy indicates the formation of Y–Cr-rich oxides along grain boundaries in the steel near the metal–oxide interface may act to block cation diffusion [26]. The inner spinel layer that forms in the ODS alloy is more porous, and the lower density, combined with a thinner oxide, leads to a smaller weight gain in the ODS material. Additionally, the ODS materials typically have smaller grain sizes than conventional ferritic–martensitic steels. The increased diffusion length along short-circuit diffusion paths may slow oxidation.

A second method that shows promise in slowing oxidation in ferritic–martensitic steels is surface

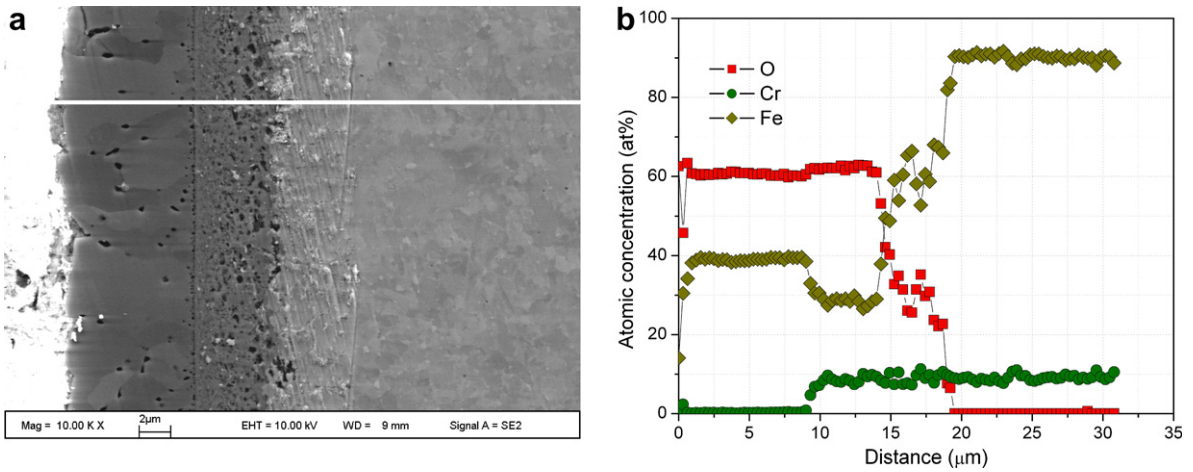


Fig. 11. (a) Cross-sectional SEM image of the 9Cr ODS ferritic steel after exposure to supercritical water at 500 °C for 1026 h and (b) corresponding composition profile across the oxide thickness [26].

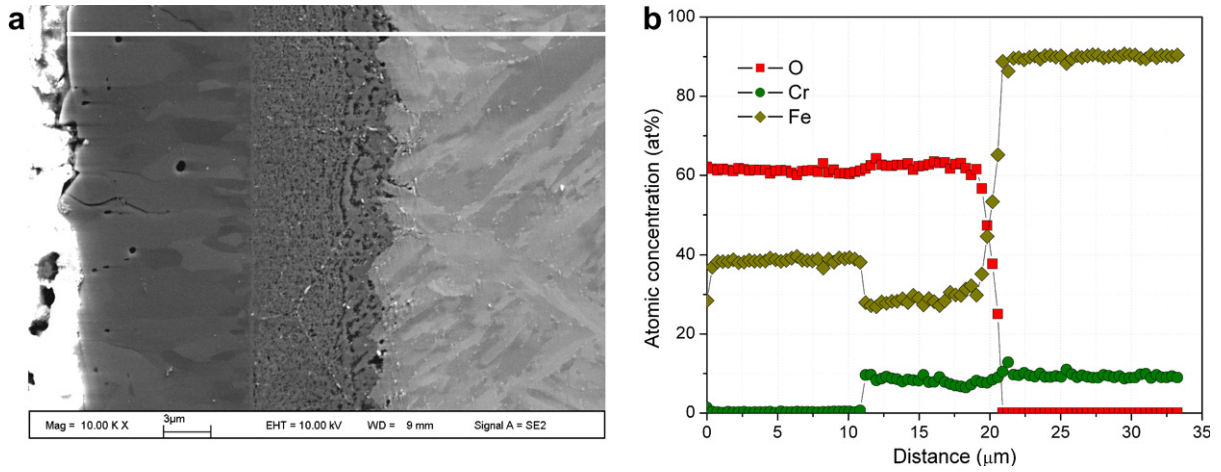


Fig. 12. (a) Cross-sectional SEM image of the 9Cr NF616 ferritic steel after exposure to supercritical water at 500 °C for 1026 h and (b) corresponding composition profile across the oxide thickness [26].

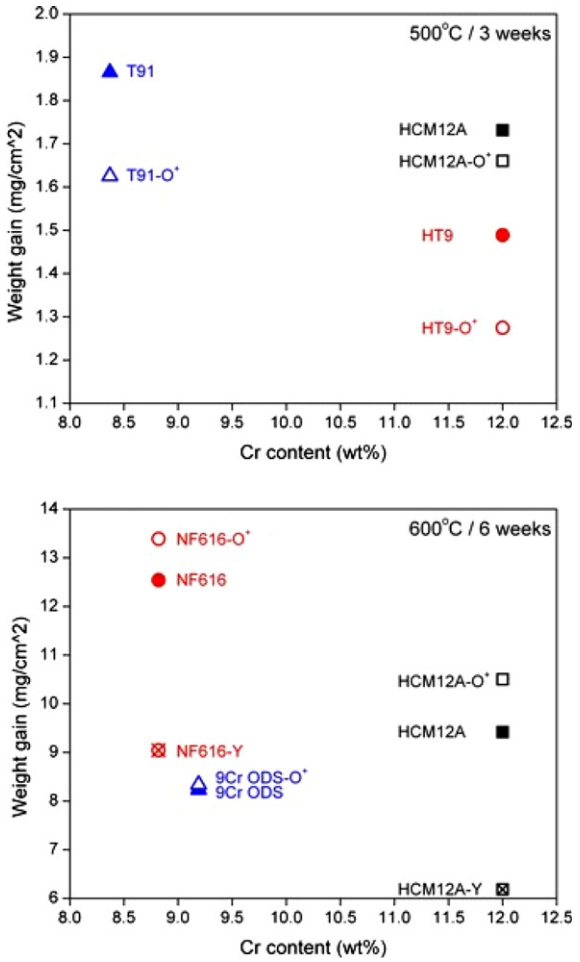


Fig. 13. Effect of oxygen and yttrium surface implantation at 500 °C, and 600 °C on T91, HCM12A, HT9, NF616, and 9Cr ODS.

composition modification. Both oxygen and yttrium have been implanted into the surface of various ferritic–martensitic steels. The change in weight gain with various surface implantation conditions is shown in Fig. 13. At 500 °C, oxygen implantation reduced the weight gain in T91, HCM12A, and HT9. The reduction in oxide thickness in HT9 has an associated change in the oxide texture early in the development of the oxide, but at longer times, the textures are similar between samples with and without oxygen pre-implantation [27]. One possible explanation for the texture is that, among randomly orientated initial grains, some with certain crystal orientations grow faster than the others to release the stress introduced by the ion implantation. A second possibility is that bombardment with oxygen ions may increase nucleation sites with certain preferred orientations at the initial stage of oxide formation, resulting in a denser textured oxide layer [17].

At 600 °C, the oxygen pre-implantation was not effective in reducing weight gain due to oxidation, but pre-implantation of yttrium strongly reduced the oxide thickness in both NF616 and HCM12A. A thin layer of yttrium is incorporated into the magnetite layer that appears to slow cation diffusion through the magnetite layer, thus reducing the oxidation by approximately 50%, Fig. 14.

### 3.2. Austenitic steels

Austenitic Fe-base steels were selected for possible use in supercritical water systems because of

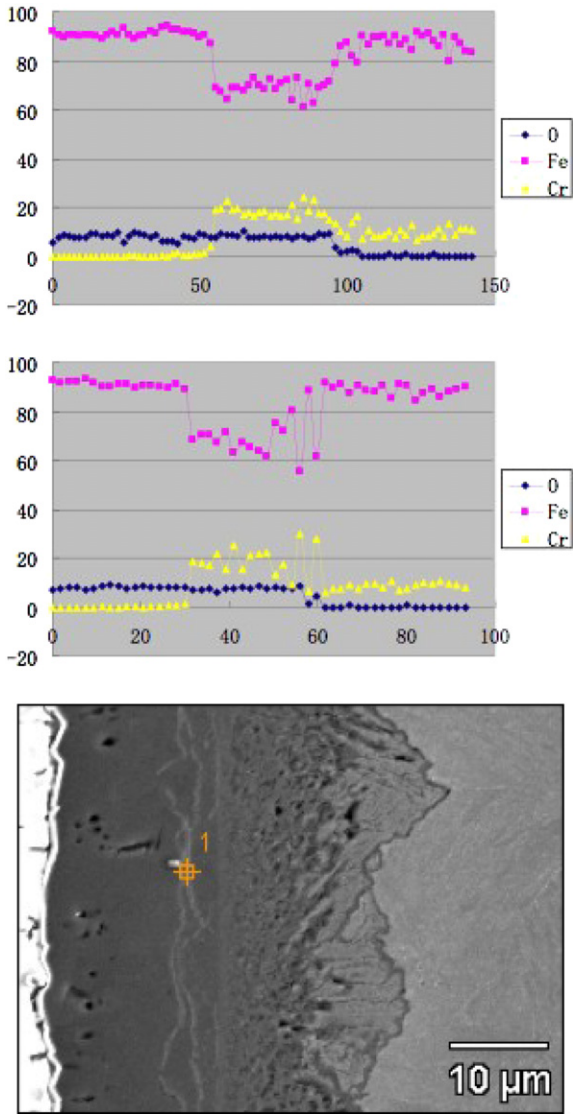


Fig. 14. Oxide thickness and compositional profile in HCM12A (top) and HCM12A with surface implantation of yttrium (middle). A thin layer of yttrium becomes incorporated into the outer magnetite layer (bottom, area marked 1) with a resulting ~50% thickness in oxide.

their corrosion resistance and relative radiation resistance compared to Ni-base alloys. To date, international programs have evaluated the following austenitic steels: 304L, 304, 304H, 316L, 316, D9, 310S, and 800H [11,13,14,28–30]. Grain boundary engineering has been performed on Alloy 800H to reduce oxide spallation.

### 3.2.1. Oxide structure

Most results on austenitic stainless steels reveal that the oxide consists of a two- or three-layer structure, consistent with that observed during exposure to air, vacuum or subcritical water [57–59]. The outer layer generally consists of magnetite with an inner layer that is rich in chromium and is either an iron–chromium spinel or an iron chromium oxide with a hematite structure [11,50,59]. As in the case of ferritic steels an internal oxidation layer is also observed between the inner oxide layer and the base metal as evidenced by a gradually decreasing oxygen diffusion profile in this transition zone.

A typical structure and composition profile for an oxide grown on an austenitic steel (800H) is shown in the SEM image in Fig. 15. The oxide structure is somewhat similar to those formed in ferritic–martensitic steels, except that the outer oxide layer is composed of both magnetite and hematite. An additional difference between austenitic and ferritic–martensitic steels is the stability of the outer oxide layer. In many of the austenitic stainless steels with higher bulk concentrations of nickel and chromium, the outer oxide layer has a tendency to spall, as demonstrated in the plan view images from D9 exposed to 500 °C 2000 ppb SCW as shown in Fig. 16.

### 3.2.2. Oxide kinetics

Austenitic stainless steels have a smaller weight gain than ferritic–martensitic steels [11,13,56]. An example of typical kinetics for tests to 1026 h is

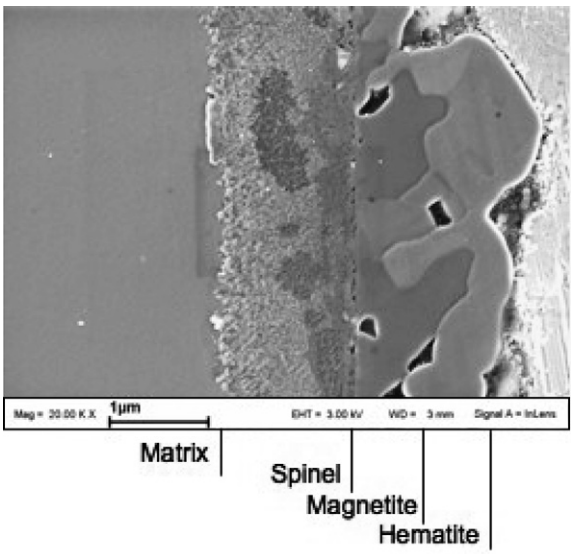


Fig. 15. Cross-section of oxide formed on Alloy 800H exposed to 500 °C SCW with 25 ppb dissolved oxygen concentration for 505 h [31].

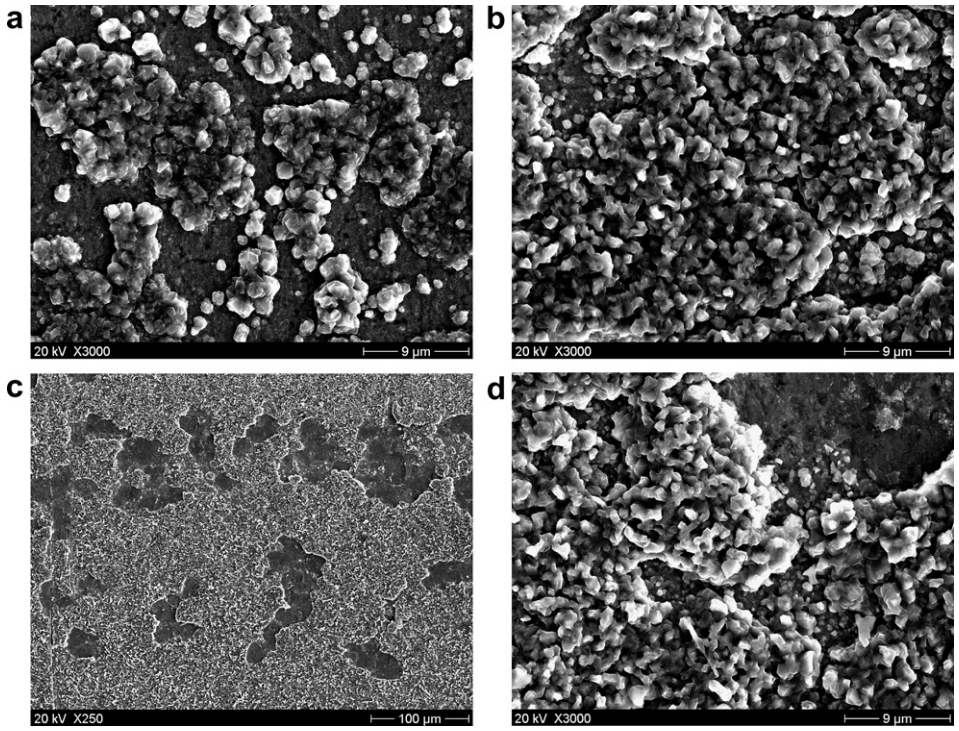


Fig. 16. SEM morphologies of the D9 samples after exposure to 2000 ppb SCW at 500 °C for (a) 168 h, (b) 335 h and (c,d) 503 h [60].

shown in Fig. 17 for alloy D9. For 500 °C and 600 °C, the oxide kinetics appear parabolic, but the data scatter is greater in austenitic alloys than in ferritic–martensitic steels. In some austenitic alloys, a portion of this scatter is attributed to spallation. The oxidation rate in austenitic alloys is smaller than in ferritic–martensitic alloys. Comparing Figs. 7 and 17, at 600 °C the oxidation at 1026 h is roughly a factor of 4 larger in HCM12A than in D9.

Like ferritic–martensitic steels, the oxidation rate increases dramatically with increasing temperature. The temperature dependence of alloy D9 is shown in Fig. 18. Because of spallation, as evidenced for D9 in Fig. 19, a simple relation between oxide thick-

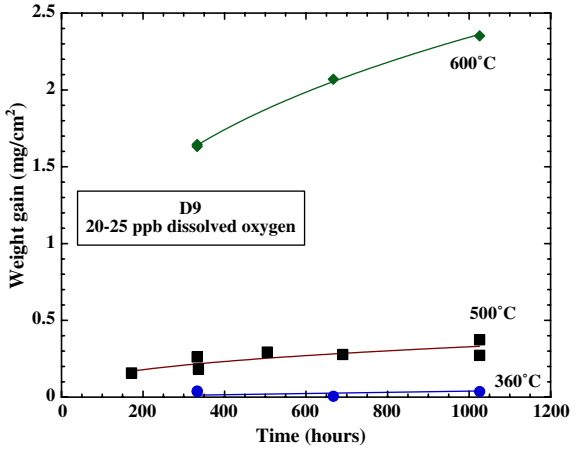


Fig. 17. Weight gain as a function of time for D9 exposed to low oxygen concentration supercritical water at 360 °C, 500 °C, and 600 °C [11].

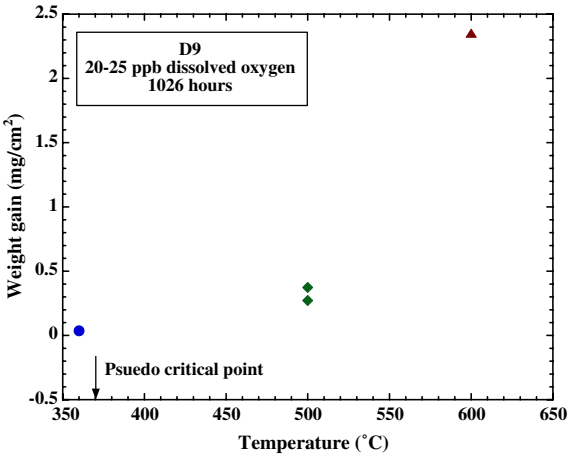


Fig. 18. Weight gain as a function of temperature for D9 exposed to low oxygen concentration supercritical water for 1026 h [11].

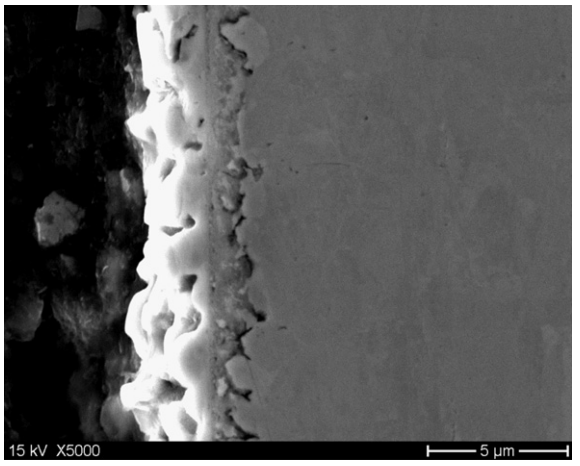


Fig. 19. Oxide thickness for D9 exposed to 500 °C SCW at 25 ppb dissolved oxygen for 1026 h [60].

ness and weight gain is not possible in many austenitic alloys. Activation energy has been calculated for some austenitic steels, specifically 210 kJ/mol for 304L and 214 kJ/mol for 316L, higher than the energy measured in T91, HCM12A, and HT9.

### 3.2.3. Effect of dissolved oxygen

The effect of dissolved oxygen is more complex in austenitic alloys than in ferritic–martensitic steels. This is demonstrated in Fig. 20 for D9 and 21 for 316 and 316L. For D9 exposed at 500 °C, at short times, the weight gain is smaller at very high (2000 ppb) dissolved oxygen than at low (25 ppb dissolved oxygen). At longer times (between 333 and 505 h), the oxidation rate of the D9 exposed to 2000 ppb dissolved oxygen increases significantly. It is noted for the D9 samples exposed to 25 ppb oxygen content, particularly for longer exposure times that the weight gain remains nearly constant, an affect that is attributed to oxide spallation in these alloys. The weight gain measurements shown in Fig. 20 represent the cumulative effects of weight gain due to oxidation as well as spallation. The weight loss due to spallation counterbalances the weight gain due to the growth of the oxide layer. This observation is supported by our SEM observations of oxide spallation in D9 steels. It is speculated that this effect would be observed for the samples exposed to higher oxygen SCW if the samples had been exposed to longer durations.

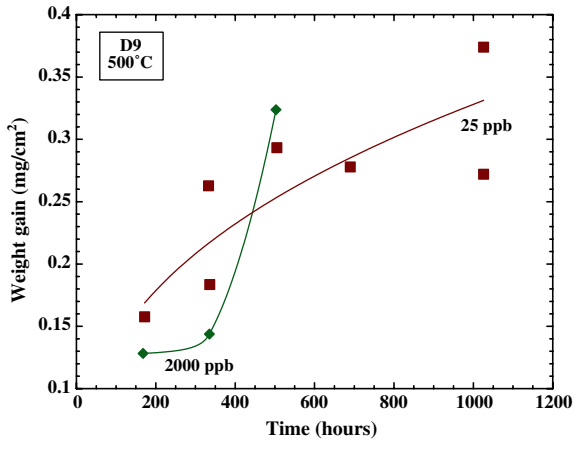


Fig. 20. Weight gain as a function of time for D9 exposed to 25 ppb and 2000 ppb oxygen concentration at 500 °C [11].

Weight gain rate for 316 and 316L as a function of temperature from this work is compared to that of Kasahara et al. [13], who exposed 316L in a static autoclave at 8000 ppb dissolved oxygen, in Fig. 21. At low temperatures, the oxidation is minimal and no significant difference is noted between 316 and 316L or between exposures at different oxygen concentration. At 500 °C, higher dissolved oxygen leads to greater weight gain in 316. At 550 °C, the weight gain rate is actually higher for the deoxygenated (<10 ppb) case than for the 8000 ppb case.

The effect of oxygen is not as straightforward in the austenitic steels as was seen in the ferritic–martensitic steels and greater study is needed to identify

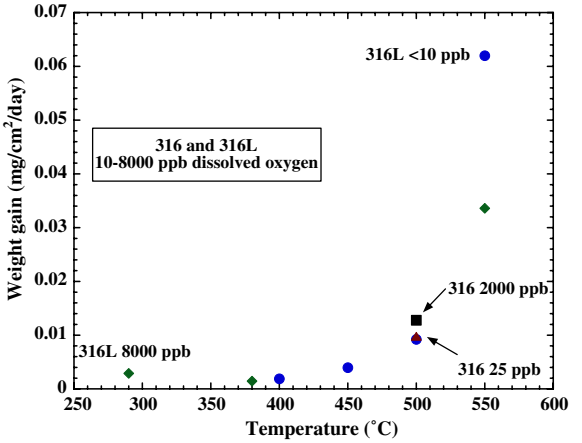


Fig. 21. Weight gain rate as a function of temperature for 316L exposed in <10 ppb dissolved oxygen (blue circles), 316L exposed in 8000 ppb dissolved oxygen (green diamonds), 316 exposed in 25 ppb dissolved oxygen (red triangles), and 316 exposed in 2000 ppb dissolved oxygen (black squares) [11,13]. (For interpretation of the references in colour in this figure legend, the reader is referred to the web version of this article.)

the optimal oxygen concentration to minimize oxidation.

### 3.2.4. Effect of alloy composition

The trends in weight gain as a function of time for three austenitic alloys exposed to 20–25 ppb dissolved oxygen are shown in Fig. 22 for 500 °C and Fig. 23 for 600 °C exposures. The weight gain is always the smallest for 800H, but the fluctuations in weight gain are indicative of the oxide spallation that occurs on this alloy. The relative weight gain of 316 and D9 differ as temperature varies. D9 has a greater weight gain at 500 °C and 316 has a greater weight gain at 600 °C.

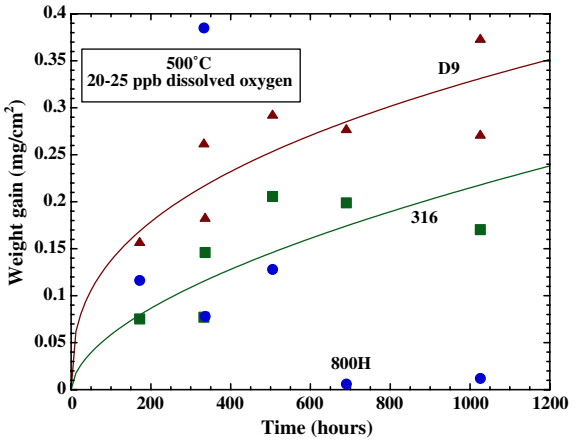


Fig. 22. Weight gain as a function of time for D9, 316, and 800H exposed to low oxygen concentration supercritical water at 500 °C [11].

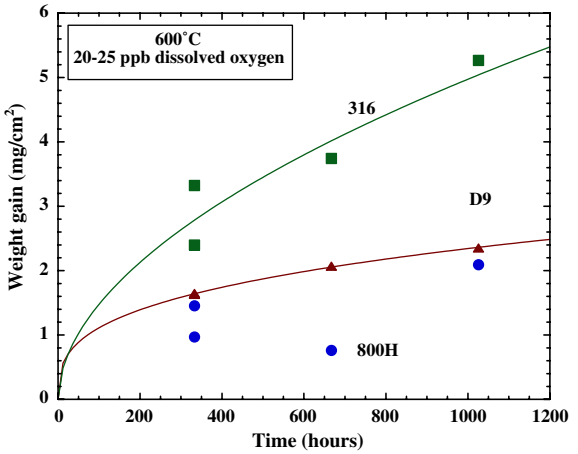


Fig. 23. Weight gain as a function of time for D9, 316, and 800H exposed to low oxygen concentration supercritical water at 600 °C.

The effect of bulk composition is not as straightforward in the austenitic steels as was seen in the ferritic–martensitic steels and greater study is needed to identify optimal alloying concentrations required to form thin stable oxides.

### 3.2.5. Spallation reduction methods

Grain boundary engineering (GBE) was applied to Alloy 800H by means of thermomechanical processing to improve protective oxidation behavior [31]. Control (annealed) and GBE-treated alloy 800H samples were exposed in supercritical water with 25 ppb dissolved oxygen at 500 °C and 25 MPa. Results indicate that extensive oxide spallation occurred on control samples but not on GBE-treated samples, Fig. 24. This trend holds at both 500 °C and 600 °C. A dual-layer structure of oxide scale formed on both control and GBE-treated samples with the outer layer composed of hematite and magnetite, and the inner layer composed of a mixture of austenite (substrate) and spinel. A relatively mild isotropic texture of oxide, smaller hematite grain size, larger hematite fraction in the oxide, and increased intermixing between the substrate and spinel were observed in GBE-treated samples by means of EBSD analyses. All of these features are believed to be beneficial for alleviating scale cracking and spallation. The protective oxidation behavior of GBE-treated samples represented by the improved spallation resistance and slower oxidation rate is believed to be attributable to the highly increased population of low-$\Sigma$ CSLBs.

## 3.3. Ni-base alloys

Ni-base alloys were selected for possible use in supercritical water systems because of their corrosion resistance and high-temperature strength. To date, international programs have evaluated the following Ni-base alloys: 625, 690, 600, 825, C276, C22, 718, B2, MAT21, and MC [11,13,14,30,32].

### 3.3.1. Oxide kinetics

The weight gain in Ni-base alloys is small compared to both ferritic–martensitic steels and austenitic steels [11,13,56]. The weight gain for alloy 625 as a function of time at 20–25 ppb dissolved oxygen and temperatures of 360 °C, 500 °C, and 600 °C is shown in Fig. 25. At 600 °C and 1026 h, the weight gain of 625 is a factor of three less than that of 316 stainless steel. In general, for times to ~1000 h, exposures at temperatures above the pseudo-critical

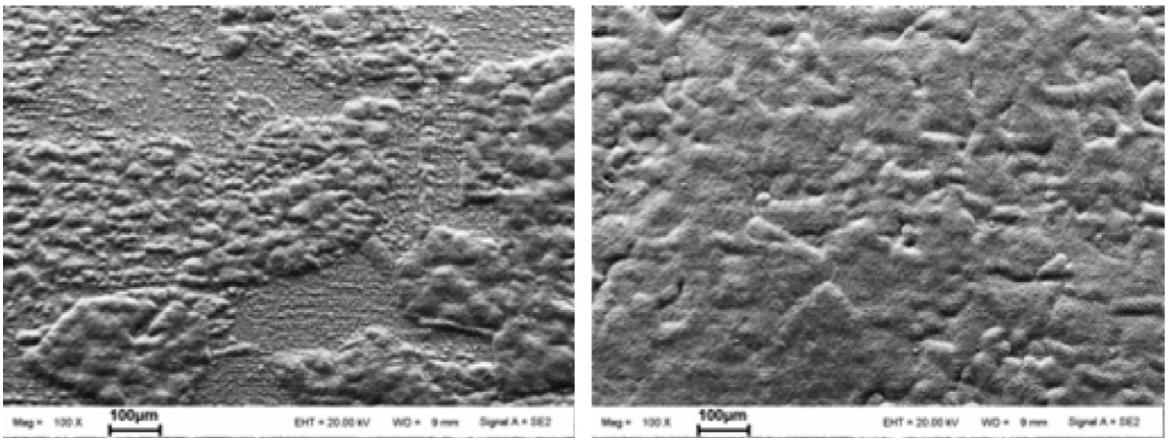


Fig. 24. Effect of grain boundary engineering on spallation in Alloy 800H exposed to supercritical water at 600 °C, 25 ppb $O_2$ for 6 weeks [31].

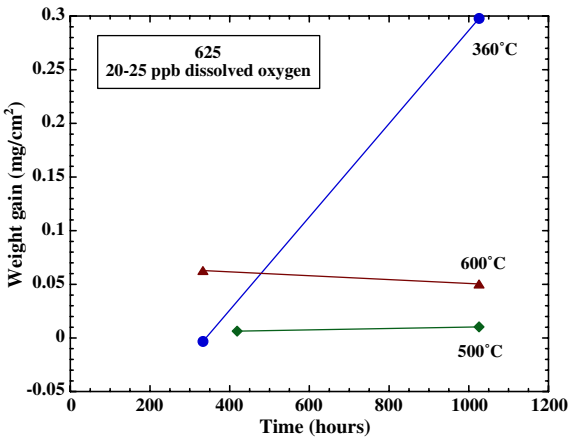


Fig. 25. Weight gain as a function of time for 625 exposed to low oxygen concentration supercritical water at 360 °C, 500 °C, and 600 °C [11,61].

point, and under low oxygen concentration, the weight change for all Ni-base alloys is small, fluctuating, and not experiencing any significant growth. For temperatures from 400 to 550 °C, the activation energy for oxidation for alloy 690 was calculated to be 134 kJ/mol [11]. Ni-based alloys are the only alloy class where a higher weight gain due to oxidation is observed in the subcritical water temperature of 360 °C. It should be noted here that the density of water drops dramatically at the critical temperature and the subcritical water at 360 °C has a significantly higher than supercritical water at 500 °C and 600 °C. This may play a role in the higher weight gain observed for Ni-based alloys at this subcritical temperature. The weight gain at 360 °C for 625 is similar to that of D9 exposed at 500 °C for 1026 h.

The oxide layers in Ni-base alloys exposed for times to 1026 h are very thin, such that cross-section views cannot typically be prepared. Pitting may also occur in precipitation-hardened alloys. Plan view images of alloy 625 show a thin layer of general corrosion along with pitting, Fig. 26. Some of the fluctuations in weight gain seen in Ni-base alloys are caused by the competing processes of weight gain due to oxidation and weight loss due to pitting. Subtracting the weight loss due to pitting allows for an estimation of the weight gain and oxide thickness in alloy 625, Table 2.

### 3.3.2. Oxide structure

Even though the oxides of Ni-base alloys are too thin to be examined using cross-sectional SEM techniques, details of the oxide structure can be determined using plan view imaging and sputter depth profiling. An example is shown in Fig. 27 for alloy 625 exposed to 25 ppb SCW at 600 °C for 1026 h. In these EDS mapping images, different colors are used to show the different chemical elements, oxygen and chromium and nickel in this case, and the brightness of each color corresponds to the concentration of each element. The color scale bar with the minimum and maximum counts is shown above each image. On the oxide surface, oxygen and chromium were enriched at grain boundaries and nickel was depleted. Using argon ion milling, the layer just beneath the surface of the oxide was investigated. The oxide layer was sputtered off for around 25 minutes and the oxide removal was confirmed by the absence of oxide peaks in the AES spectrum. The surface morphology of the sputtered surface is

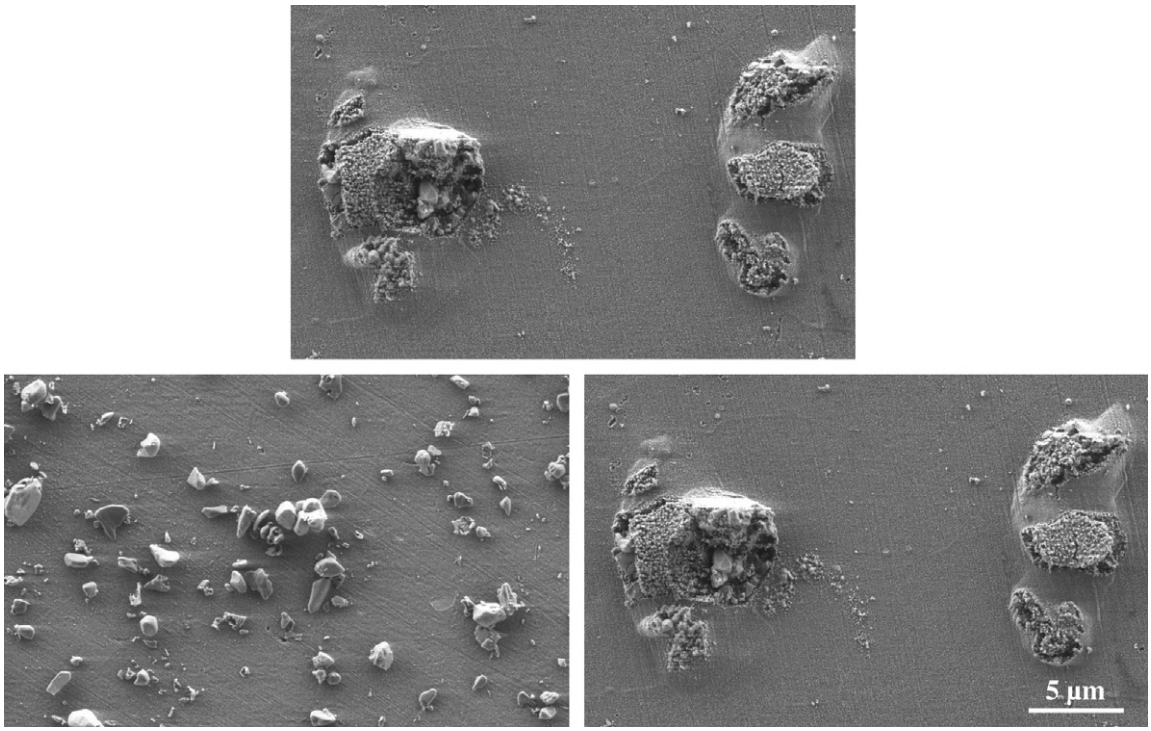


Fig. 26. Surface morphology of alloy 625 samples exposed to SCW at 25 ppb dissolved oxygen at 500 °C for around 500 h. General corrosion is seen in the left image and pitting corrosion in the right image [61].

Table 2
Weight gain adjusted for mass loss due to pitting in alloy 625 [11]

| | 400 °C | 450 °C | 500 °C | 550 °C |
|---|---|---|---|---|
| Average pit diameter (μm) | 5.29 | 4.03 | 5.46 | 5.31 |
| Number density (#/mm$^2$) | 226 | 102 | 344 | 117 |
| Weight loss due to pitting (mg/dm$^2$) | 0.93 | 0.16 | 1.82 | 0.54 |
| Measured weight gain (mg/dm$^2$) | −0.50 | 0.75 | 0.63 | 2.5 |
| Weight gain due to oxidation (mg/dm$^2$) | 0.43 | 0.91 | 2.45 | 3.04 |
| Oxide thickness (μm) | NM | NM | 0.13 | 0.15 |

shown in Fig. 27 (right column, after sputtering). The chromium is depleted at metal grain boundaries, while a slight enrichment of nickel was observed. The grain boundaries are the primary route for delivering chromium to the surface, leading to Cr-rich oxides preferentially forming above the grain boundaries and Cr-deficient grain boundaries at the metal surface.

### 3.4. Zr-base alloys

Zirconium-base alloys can be considered for some supercritical water reactor applications because of their good neutron economy. Alloys investigated in international programs include Zircaloy-2, Zircaloy-4, zirconium, and model alloys including Zr–Nb, Zr–Fe–Cr, and Zr–Cu–Mo [33–36].

Initial studies on Zircaloy-2 and Zircaloy-4 showed extreme oxidation and indicated zirconium-base alloys would be unacceptable at the temperatures required in a SCW-cooled system. Further studies on model alloys [36] have indicated that optimized compositions can reduce the oxidation rate to levels less than ferritic–martensitic steels and greater than austenitic steels. The high-temperature strength of zirconium-base alloys is not yet sufficient for high stress components.

### 3.5. Ti-base alloys

Japanese programs have studied the corrosion of Ti-base alloys in SCW. Alloys examined include Ti–15Mo–5Zr–3Al, Ti–3Al–2.5V, Ti–6Al–4V, and Ti–15V–3Al–3Sn–3Cr [28]. These Ti-base alloys were exposed in static autoclaves with 8000 ppb dissolved oxygen for 500 h at temperatures of 290°, 380°, and 550 °C. Little difference was noted in the weight

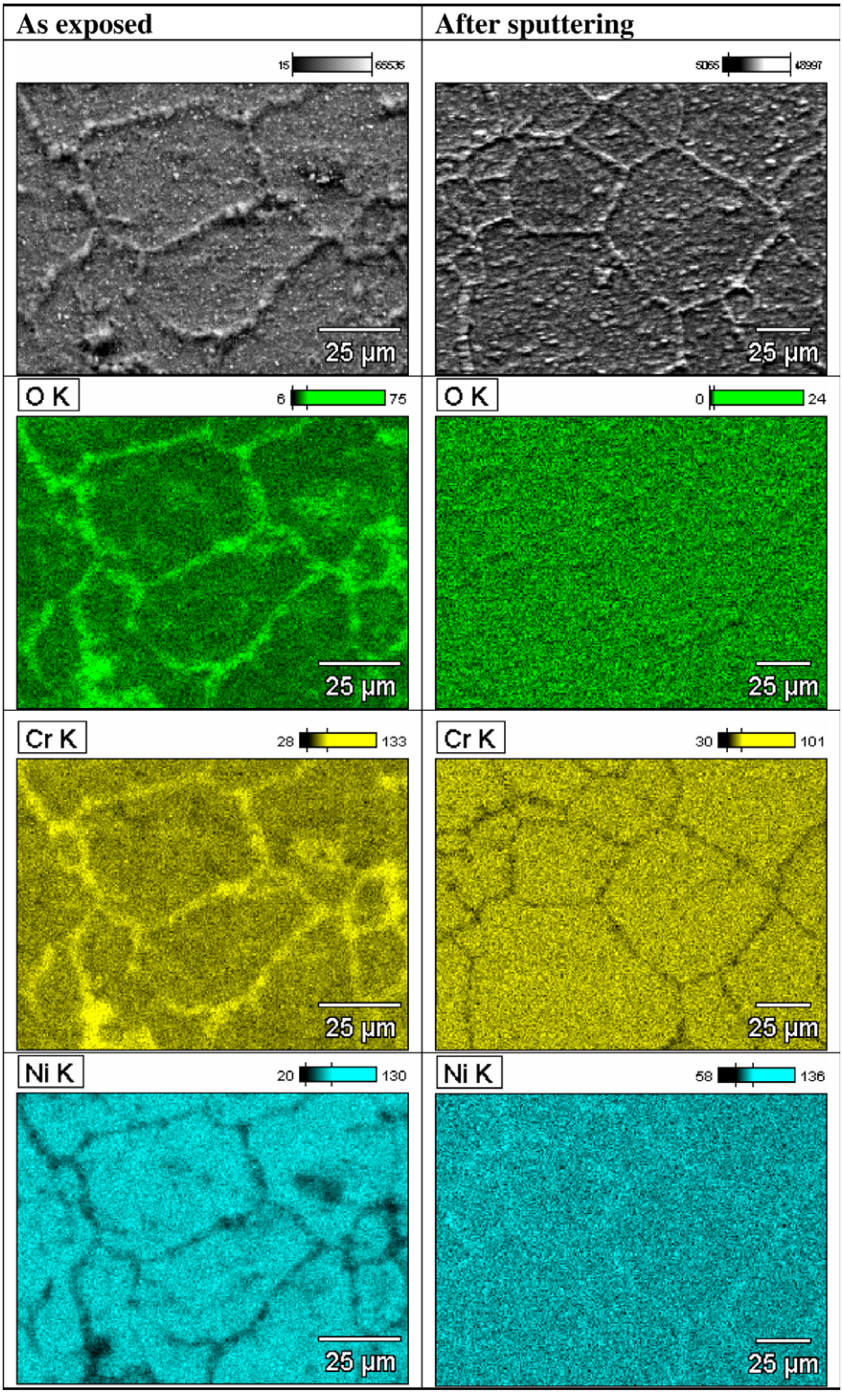


Fig. 27. Intergranular corrosion observed in 625 exposed to 25 ppb SCW at 600 °C for 1026 h (left column, as exposed). 'After sputtering' shows the layer just beneath the oxide layer exposed by removing the oxide layer through argon ion milling [61].

gain of samples exposed at 290 °C and 380 °C. The weight gain of the samples exposed at 550 °C was significantly higher than that of the samples exposed at lower temperature. At 550 °C, the Ti–15V–3Al–3Sn–3Cr and Ti–15Mo–5Zr–3Al alloys had roughly a factor of three lower weight gain than the Ti–3Al–2.5V and Ti–6Al–4V alloys. The weight gain at 550 °C in Ti–15V–3Al–3Sn–3Cr is similar to the weight gain experienced by 304 stainless steel exposed at the same temperature and <10 ppb dissolved oxygen.

### 3.6. Corrosion summary

The following trends are noted in the response of various alloy classes exposed to SCW for times to 1026 h over a temperature range of 290–600 °C.

1. Ferritic–martensitic steels form stable oxides with roughly parabolic kinetics. The weight gain in ferritic–martensitic steels is larger than any other alloy class and may limit their application in a SCW system. Increasing the bulk chromium concentration reduces the oxidation rate. An optimal oxygen concentration near 300 ppb may limit the total oxide growth. Oxide dispersion strengthened steels and steels modified by adding a thin layer of yttrium significantly reduce the oxidation rate.
2. Austenitic stainless steels show less weight gain than ferritic–martensitic steels but are more prone to spallation. The response of austenitic stainless steels as a function of alloy composition, temperature, and dissolved oxygen is complex and not as predictable as in ferritic–martensitic steels. Grain boundary engineering techniques eliminate spallation in Alloy 800H.
3. Nickel-base alloys show very little weight gain due to oxidation, except at temperatures below the pseudo-critical point where exposure to higher density fluid increases the oxidation rate significantly. Precipitate hardened alloy are prone to pitting and part of the complex changes in weight gain seen in Ni-base alloys is a competition between pitting and general oxidation.
4. Even though commercial Zircaloy alloys used in light water reactors suffer from extreme oxidation under supercritical conditions, compositionally optimized zirconium alloys have oxidation rates between those found in austenitic stainless steels and ferritic–martensitic steels.
5. Compositionally optimized titanium-base alloys have oxidation rates on par with those found in austenitic stainless steels.

## 4. Stress corrosion cracking

This section summarizes the stress corrosion cracking data in pure supercritical water or with additions of acid. These data are distinct from the body of literature covered by supercritical water oxidation (SCWO) experiments.

To date stress corrosion cracking experiments in supercritical water have been limited to constant extension rate tensile (CERT) or constant load tensile (CLT) tests. A total of 4 alloy systems have been investigated for their stress corrosion cracking response in varying levels of detail: austenitic stainless steels (5 alloys/53 samples), nickel-base alloys (8 alloys/43 samples), ferritic–martensitic steels (4 alloys/29 samples) and titanium alloys (1 alloy/1 sample). Stress corrosion cracking has been found in all but the titanium alloy system. The alloy systems, specific alloys and range of test conditions is summarized in Table 3.

The existing database is characterized by a large number of alloys and parameters and yet

Table 3
Summary of alloys and conditions used in stress corrosion cracking experiments in supercritical water

| Alloy class | Alloys | Temperature (°C) | Dissolved oxygen (ppm) | Chemical additions | Studies |
|---|---|---|---|---|---|
| Austenitic SS | 304, 316, 316L, 347, 31266 | 380–732 | <0.01–800 | $H_2SO_4$, HCl, $H_2O_2$, NaCl | [14,29,32,36–44] |
| Nickel-base | 600, 625, 690, 800H, 718, MC alloy, UNS N 06030, C-276 | 290–550 | <0.01–8 | $H_2SO_4$, HCl, $H_2O_2$, NaCl | [36–40,42,43,45,46] |
| Ferritic–martensitic | HCM12A (T122), HT-9, T91, T92 (NF616) | 400–600 | <0.01–8 | NA | [12,46–48] |
| Titanium-base | Ti–15Mo–5Zr–3Al | 290–550 | 8 | NA | [43] |

experiments were conducted by relatively few investigators and labs. The selections of the reference alloy condition (sensitized vs. unsensitized) and the reference water chemistry (deaerated vs. 8 ppm dissolved oxygen) tend to be specific to the laboratory in which the experiments were conducted. The result is that there exist few instances in which data can be compared between laboratories due to the inherent differences in the experimental conditions. As such, the following results and their interpretation are compromised somewhat by the lack of a systematic approach across the various laboratories and investigators conducting the experiments.

### 4.1. Austenitic stainless steels

Austenitic stainless steels that have been tested in pure supercritical water include 304, 316, 316L, 347 and UNS S31266. All of these alloys have experienced some degree of stress corrosion cracking, most of which is intergranular. Figs. 28 and 29 show the maximum stress and the strain to failure for several stainless alloys tested in CERT mode in SCW. Note that there is a general decrease in the maximum stress with temperature, but the strain to failure does not show a clear trend. These data sets consist of essentially two groups of data, those for CERT tests conducted on sensitized alloys in 8 ppm dissolved oxygen and a set consisting of solution annealed samples tested in deaerated (<10 ppb $O_2$).

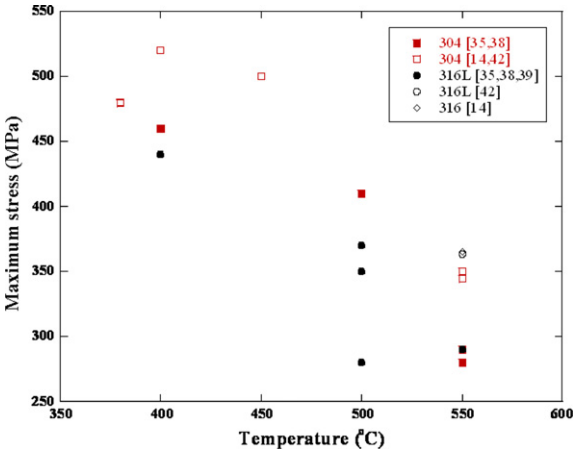


Fig. 28. Maximum stress vs. temperature in CERT tests on austenitic stainless steel in supercritical water. Solid symbols denote on solution annealed samples in deaereated SCW, and open symbols denote sensitized samples in 8 ppm dissolved oxygen.

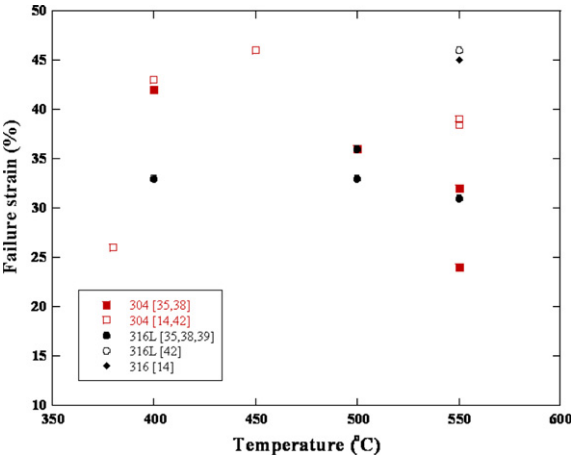


Fig. 29. Strain to failure vs. temperature in CERT tests on austenitic stainless steel in supercritical water. Solid symbols denote on solution annealed samples in deaereated SCW, and open symbols denote sensitized samples in 8 ppm dissolved oxygen.

#### 4.1.1. Alloy and temperature

A plot of the incidence of stress corrosion cracking as a function of alloy and temperature is given in Fig. 30. Two trends emerge depending on how the cracking behavior is characterized. Tsuchiya et al. [14] and Fujisawa et al. [37] use the %IG on the fracture surface as a measure of SCC susceptibility. Was

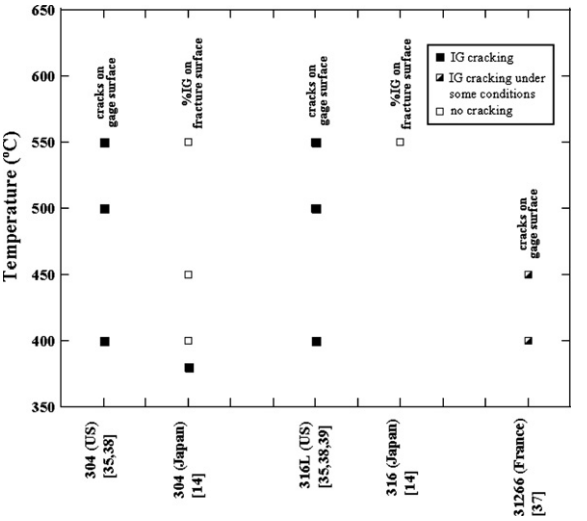


Fig. 30. Dependence of SCC susceptibility reporting on the type of measurement; cracking on the gage surfaces vs. %IG on the fracture surface. Note that gage surface cracking measurements were made on solution annealed samples in deaerated SCW and %IG on fracture surface measurements were made on sensitized samples in 8 ppm dissolved oxygen.

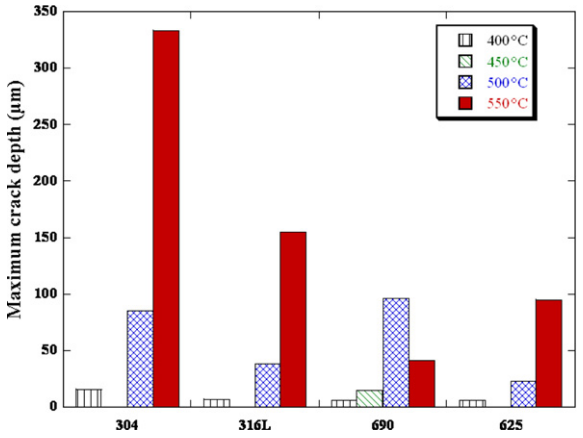


Fig. 31. Crack depth of austenitic alloys and stainless steels as a function of temperature following CERT testing in pure, deaerated (<10 ppb $O_2$) supercritical water [36].

et al. [36,39,40] use the crack depth and the crack density on the gage surface as an indicator of the IGSCC susceptibility. Unfortunately, these measures are not always in agreement. %IG requires significant crack growth to be observed. However, crack density is more sensitive to small cracks and may capture crack initiation better. Was et al. noted that in annealed 304 and 316L in deaerated SCW, the cracking severity as measured by the crack depth increased with temperature, Figs. 32 and 33, but the %IG amounted to only a few percent. The crack depth measurements permitted the determination of the activation energy for crack growth to be in the range 85–105 kJ/mol for the stainless steel alloys. The cracking mechanism will be discussed in more detail in the section on nickel-base alloys. Tsuchiya et al. [14] noted that IGSCC susceptibility measured as %IG on the fracture surface of sensitized 304 in 8 ppm $O_2$ dropped from 100% at 290 °C to 0% at and above 400 °C, Fig. 34, but there was a significant crack density up through 550 °C. While the alloy condition and the dissolved oxygen

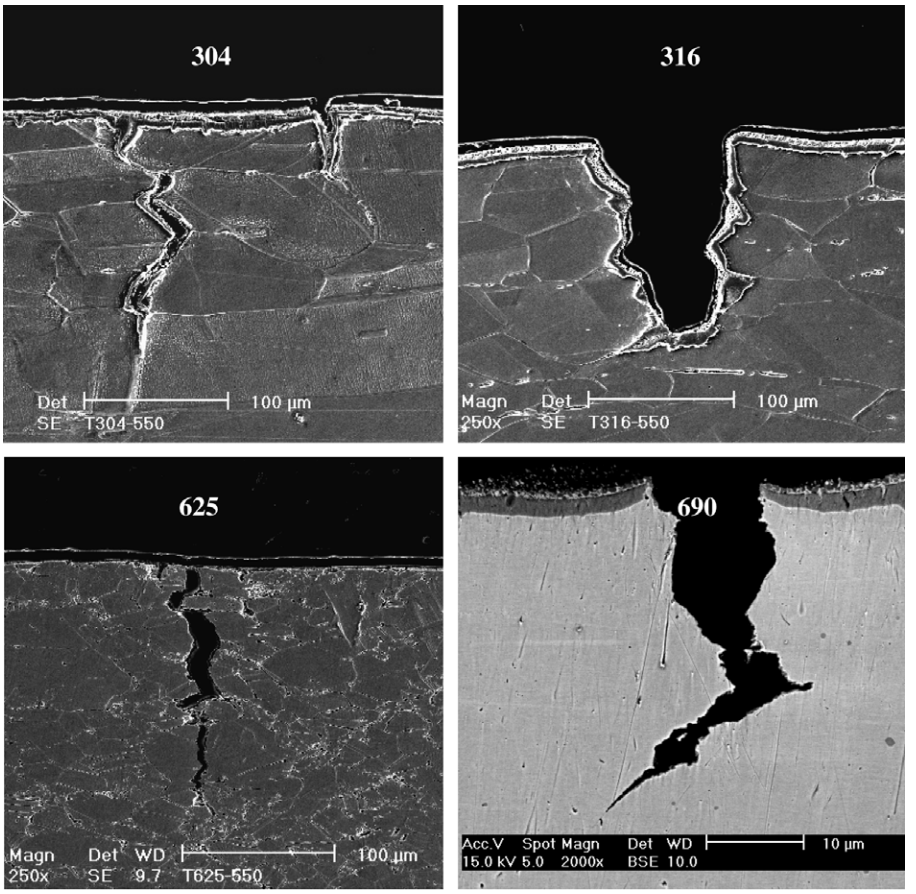


Fig. 32. Micrographs of crack morphologies on cross-sections of samples tested in pure, deaerated supercritical water at 550 °C, (a) 304, (b) 316L, (c) 625 and 500 °C (d) 690.

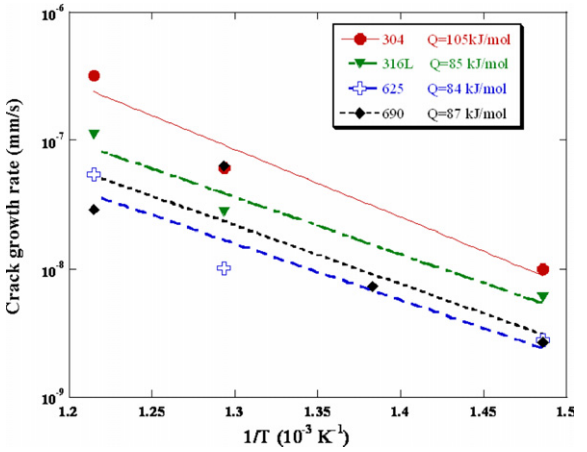


Fig. 33. Arrhenius behavior of crack growth rates and activation energy for cracking for austenitic stainless steels and nickel-base alloys tested in pure, deaerated (<10 ppb $O_2$) SCW. Rates were determined from crack depth and test time in CERT experiments.

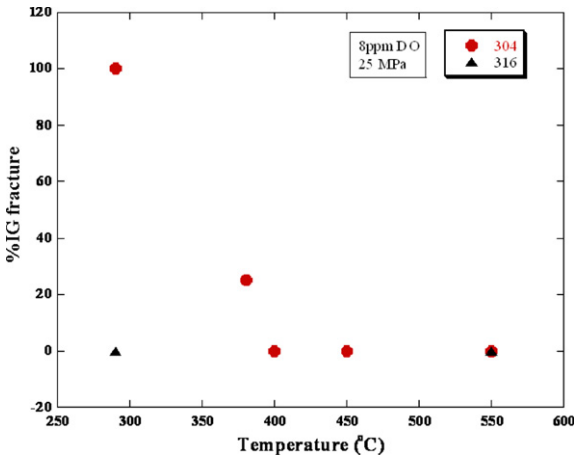


Fig. 34. %IG cracking on the fracture surface of sensitized 304 and 316L stainless steel tested in supercritical water containing 8 ppm $O_2$ [14].

content differ, these observations suggest that the %IG on the fracture surface is insufficient to characterize the full extent of SCC in SCW. While the significance of cracking on the gage surface is unknown, the degree of IG cracking is well known to depend on the strain rate in CERT tests and at lower strain rates, the amount of IG cracking could increase substantially. However, a systematic analysis of the effect of strain rate on IGSCC in SCW has not yet been conducted. Therefore, both measures of IG cracking propensity, %IG on the fracture surface and crack density on the gage surface, should be considered.

#### 4.1.2. Water chemistry additions

Several studies have been conducted on the effect of additions to SCW including $H_2SO_4$, HCl, NaCl and $H_2O_2$. The addition of HCl to 400 °C SCW containing 8 ppm dissolved oxygen resulted in a decreased strain to failure and increased IGSCC susceptibility in 316SS over the range 0.001–0.01 mol/l [37]. Addition of 0.01M $H_2SO_4$ to SCW resulted in a sharp reduction in strain to failure in solution annealed 316L stainless steel and severe intergranular cracking [29,32]. These results are in contrast to those of Tsichyua et al. [14], but since both the material condition and the water chemistry were different, it is unclear whether one or both are responsible for the difference. Results do match those of Was for solution annealed 316L stainless steel [36,40].

Two other austenitic stainless steels, 'superaustenitic stainless steel' UNS S 31266, and type 347 were tested in supercritical water. UNS S 31266 was tested at 400 °C or 450 °C in SCW with additions of 10 wt% $H_2O_2$, 1 g/l HCl, or 10 wt% $H_2O_2$ + 1.6 g/l NaCl in both CERT mode ($5 \times 10^{-7}$ $s^{-1}$) and CLT (100% of the elastic limit) [38]. The CERT test in 400 °C SCW + 10 wt% $H_2O_2$ resulted in SCC, but the CLT test in the same environment at 450 °C showed no evidence of cracking. However, CLT tests in 10 wt% $H_2O_2$ + 1.6 g/l NaCl at 450 °C and in 1 g/l HCl at 400 °C resulted in cracks ranging from 5 to 130 μm in length. Alloys 316 and 347 were exposed to 732 °C, 34.5 MPa SCW and stressed to 90% of the stress required to cause rupture in 1000 h (103 MPa) [41]. After one week of exposure, the 316 sample had failed and exhibited several small cracks in addition to the crack that caused failure.

#### 4.1.3. Pressure

Watanabe [29,32] conducted a systematic study of the effect of SCW pressure on the cracking propensity of sensitized 316 stainless steel in pure water containing 8 ppm dissolved oxygen. Varying the water pressure from 25 to 60 MPa at 400 °C, he observed a monotonic decrease in strain to failure and maximum stress and an increasing amount of IG fracture with pressure, Fig. 35. By 60 MPa, the failure was almost totally intergranular. Watanabe suggests that the high pressure results in a higher dielectric constant condition in which ionization of metal is easier and solubility of the oxide is higher, resulting in enhanced anodic dissolution and greater

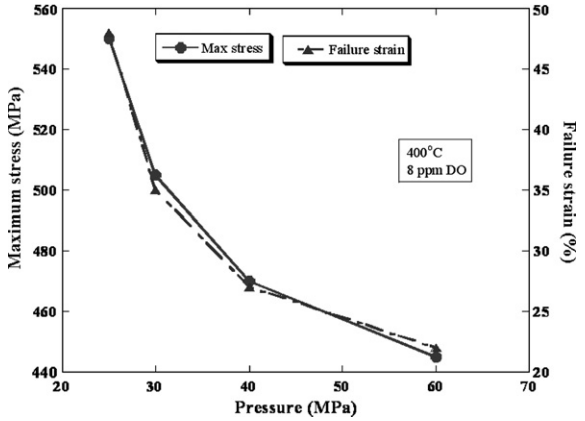


Fig. 35. Effect of system pressure on maximum stress and strain to failure for sensitized 316 stainless steel tested in CERT mode in pure supercritical water containing 8 ppm $O_2$ at 400 °C [29].

cracking propensity. The reverse is true for the low density, gas-like character of SCW at low pressure.

#### 4.1.4. Irradiation

Irradiation of 304 and 316L stainless steel significantly increased the IG cracking propensity at both 400 °C and 500 °C. Samples irradiated with 3 MeV protons to 7 dpa showed significant increases in the amount of IG cracking as measured by the crack length per unit area, Fig. 36 [44]. The effect was greater at 500 °C than at 400 °C.

Overall, austenitic alloys were observed to be susceptible to IGSCC in supercritical water where the extent of susceptibility varied with both alloy and water chemistry conditions. Higher temperature

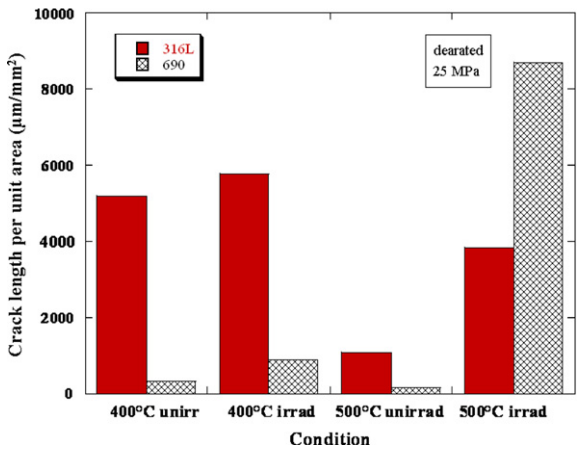


Fig. 36. Effect of 3 MeV proton irradiation to 7 dpa on crack length per unit area in 316L stainless steel and alloy 690 tested in CERT mode in pure, deaerated (<10 ppb $O_2$) supercritical water at the same test temperature as the irradiation [44].

resulted in greater cracking on the gage section but a reduction in the %IG on the fracture surface. Overall, 304 exhibits greater susceptibility than does 316 and additions of small amounts of acid to the solution increase the susceptibility. Increasing SCW pressure favors IG cracking in unsensitized 316 SS in pure water + 0.01 mol/l $H_2SO_4$.

### 4.2. Nickel-base alloys

A total of eight nickel-base alloys have been tested for stress corrosion cracking susceptibility in supercritical water, Table 2. The tests were performed at temperatures ranging from 390 to 550 °C and at pressures ranging from 22.5 to 25.5 MPa. The dissolved oxygen content was maintained either in the deaerated condition or at 500 ppb or 8 ppm. The water chemistry was altered in some tests by the addition of HCl, $H_2O_2$, NaCl, or $H_2SO_4$. Of the eight alloys tested, only the MC alloy [38] and the UNS N06030 alloy [37] did not show any evidence of SCC.

#### 4.2.1. Alloy

Alloy 718 proved to be extremely susceptible to SCC [45]. A CERT test conducted on a sample of 718 in aerated (8 ppm) SCW at 400 °C failed at a strain of only 9% and a maximum stress of 1300 MPa, and the fracture surface was completely intergranular fracture. The authors attributed this cracking behavior to the oxidation and swelling of the primary niobium carbides that cause cracks to initiate at these carbides.

CERT tests on alloy 690 have produced mixed results. Fournier et al. [45] tested 690 in 400 °C, 25 MPa SCW under aerated conditions and found that alloy 690 failed by completely ductile rupture and showed a significant amount of necking. Companion tests in air revealed behavior for each alloy that was similar to that in SCW at 400 °C. Was et al. [36,39,40] found IGSCC in alloy 690 at 400, 450, 500 and 550 °C, with the extent of cracking increasing with temperature, Fig. 31.

Very limited tests have been conducted on alloys 800H and 600. Alloy 800H was tested in CERT mode in 500 °C SCW containing 0.5 ppm dissolved oxygen [46]. The sample failed at about 38% strain and exhibited evidence of brittle type fracture over a portion of the fracture surface. Alloy 600 was tested at 290, 380 and 550 °C in water containing 8 ppm dissolved oxygen [43]. The two lower temperature experiments failed by ductile fracture with no

sign of SCC. The sample at 550 °C exhibited a crack density of about 26 cracks/mm$^2$.

The MC alloy was tested in pure SCW at 400 °C and 8 ppm and it was also tested with the addition of 0.001 mol/l HCl and 0.01 mol/l HCl. No cracks were observed on the specimen and there was no reduction in the strain to failure when the HCl additions were made.

*4.2.2. Temperature*

Fig. 31 shows the temperature dependence of IG cracking in the nickel-base alloys 625 and 690 compared to that for the stainless steels. Both alloy systems show a strong dependence on temperature with the extent of cracking rising exponentially with temperature. Fig. 33 shows that the maximum IG crack depth obeys an Arrhenius behavior with activation energy of between 84 and 87 kJ/mol. These values are within the range of activation energies for cracking of nickel-base alloy 600 in low potential primary water in pressurized water reactors, for which the activation energy for crack growth rate in the temperature range 310–420 °C is between 80 and 220 kJ/mol [49]. The low value of the activation energy for crack growth compared to oxide growth (~200 kJ/mol) [50] may indicate either a role of aggressive species in the water or a short-circuit growth path, e.g., grain boundary oxidation ahead of the growing crack. Besides a slip-oxidation mechanism, this latter mode could also occur by selective internal oxidation (SIO) that has been observed in nickel-base alloys, as described by Scott [51], at the upper end of the temperature range used in this study. In fact, the measured crack growth rates are consistent with the diffusion of oxygen in nickel by Woodford [52]. These results show that both slip-oxidation and SIO are possible mechanisms for IGSCC in SCW.

The temperature dependence of the maximum stress and strain to failure for all of the data on nickel-base alloys is shown in Figs. 37 and 38. Perhaps because of the wide range of conditions, there is little observable dependence on temperature for either parameter. However, as shown in the preceding paragraph, samples tested within a single program tend to show a cleaner correlation.

*4.2.3. Water chemistry additions*

Fujisawa et al. [37] studied SCC of C-276, 625 and MC alloy in 400 °C SCW containing 8 ppm dissolved oxygen. No IG cracks were observed in alloy C-276 in pure water, but the addition of small

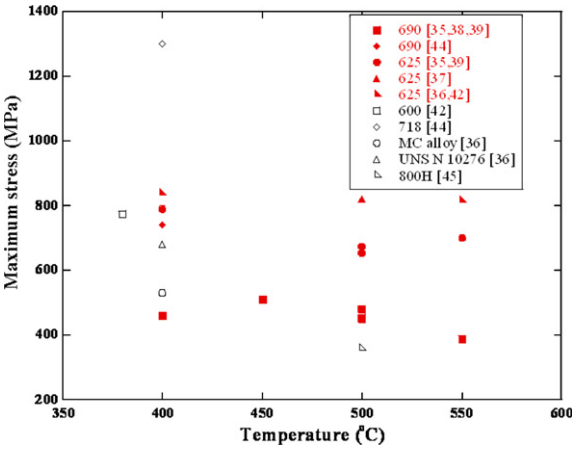


Fig. 37. Maximum stress vs. temperature in CERT tests on nickel-base alloys in supercritical water.

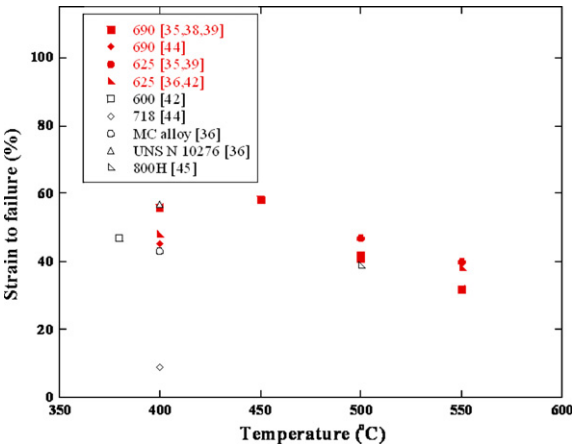


Fig. 38. Strain to failure vs. temperature in CERT tests on nickel-base alloys in supercritical water.

amounts (0.001 mol/l) HCl resulted in severe IG cracking. Alloy 625 failed by IGSCC at 0.01 mol/l HCl but not at lower concentrations or in deionized water. Bosch et al. [38] also found that 625 cracked intergranularly at both 390 °C and 450 °C in constant load tests in water containing 10 wt% $H_2O_2$ + 1.6 g/l NaCl. CERT tests in SCW + 10 wt% $H_2O_2$ revealed IG cracking at both at 400 and 500 °C with considerably greater cracking at 500 °C. No cracks were found in the MC alloy after CERT tests in 0.01 mol/l HCl at 400 °C and 8 ppm dissolved oxygen.

Alloy UNS N 06030 was tested in constant load mode (80% or 100% of yield strength) in SCW containing either 10 wt% $H_2O_2$ or 10 wt% $H_2O_2$ + 1.6 g/l NaCl at 400–450 °C [38]. No cracking was

observed in the solution containing only hydrogen peroxide and only localized corrosion, but no cracking, was observed in the latter solution.

Fujisawa showed that IGSCC susceptibility generally follows the inverse of the alloy chromium content in SCW containing HCl additions, with the austenitic stainless steel alloys exhibiting the greatest amount of IGSCC and the high nickel, MC alloy the least, Fig. 39. However, Was et al., observed that alloy 625 exhibited the worst in IGSCC resistance among 304, 316L, 625 and 690 tested in pure, deaerated SCW.

#### 4.2.4. Irradiation

Irradiation effects on nickel-base alloys is confined to alloy 690 and both 400 °C and 500 °C with 3 MeV protons to a dose of 7 dpa [44]. As shown in Fig. 36, the crack length per unit area increases substantially between the unirradiated and irradiated conditions. The difference in cracking is greatest at 500 °C where the crack length per unit area is 50x greater in the irradiated side of the sample than on the unirradiated side of the sample.

The nickel-base alloys exhibit much the same dependence of cracking on key experimental parameters as do the austenitic stainless steels. However, cracking is generally more severe in some of the alloys such as alloy 625. Chromium content appears to be a significant factor in cracking in SCW containing low concentrations of HCl. Also, irradiation has a larger effect on cracking in alloy 690 than it does on 316L stainless steel.

### 4.3. Ferritic–martensitic alloys

Four F–M alloys have been tested in SCW to date: T91, T92, HCM12A and HT-9. Of these alloys, the only one that showed susceptibility to SCC was HT-9 [12,43,46,48]. The crack densities on HT-9 (2–18 $mm^{-2}$) were generally much lower than the crack densities in the austenitic stainless steels and Ni-base alloys. Tests on F–M alloys were conducted in pure water with dissolved oxygen contents ranging from the deaerated condition (<10 ppb) to 500 ppb and temperatures ranging from 400 to 600 °C. The strains to failure of the F–M alloys were much lower than those in the austenitic alloys, ranging from 10.9% to 24.4%. One CERT test was performed on a sample of T91 in argon at 500 °C and the strain to failure was still only 15%.

HT-9 shows increasing susceptibility to cracking with temperature and dissolved oxygen content. Fig. 40 shows that both the crack density and the crack depth increase with temperature between 400 °C and 600 °C and with dissolved oxygen between 10 ppb and 300 ppb [48]. Cracking is aggravated by both high-temperature and dissolved oxygen in SCW.

Although cracks were not observed on any of the T91, T92 or HCM12A samples, it is important to note that they did show a substantially lower strain to failure with increasing dissolved oxygen in SCW. Fig. 41 shows the effect of oxygen content on strain to failure at 500 °C.

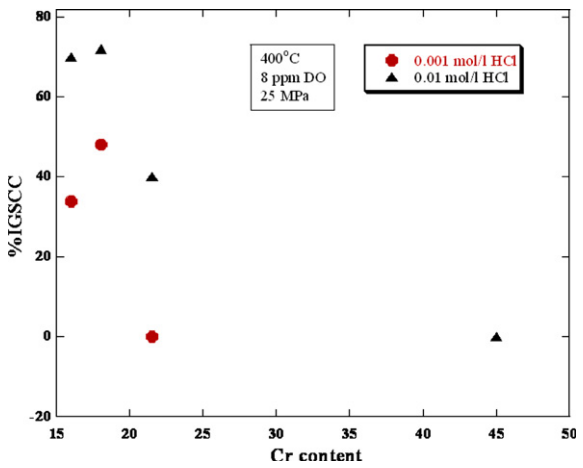


Fig. 39. Effect of the chromium content of various nickel-base alloys on the %IGSCC in 400 °C supercritical water containing 8 ppm dissolved oxygen additions of HCl [37].

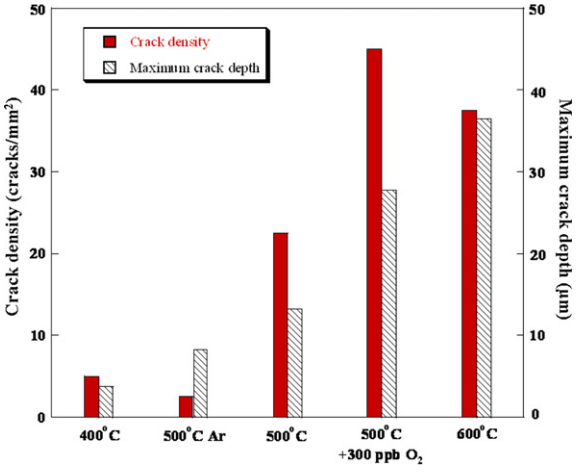


Fig. 40. Effect of temperature and dissolved oxygen content on crack density and crack depth in HT-9 tested in CERT mode in nominally deaerated SCW or in 500 °C Ar [48].

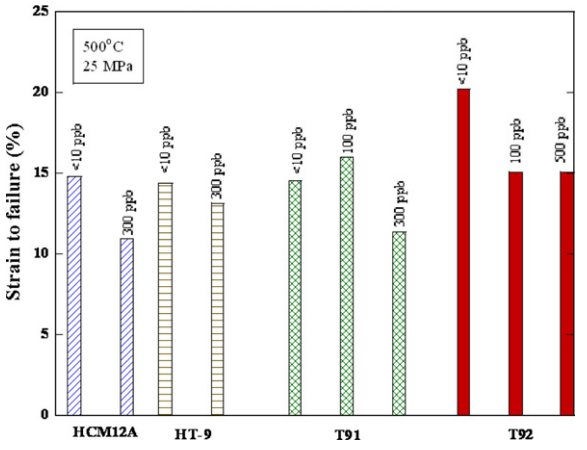


Fig. 41. Strain to failure vs. oxygen content in F–M alloys tested in CERT mode in supercritical water at 500 °C [12,46].

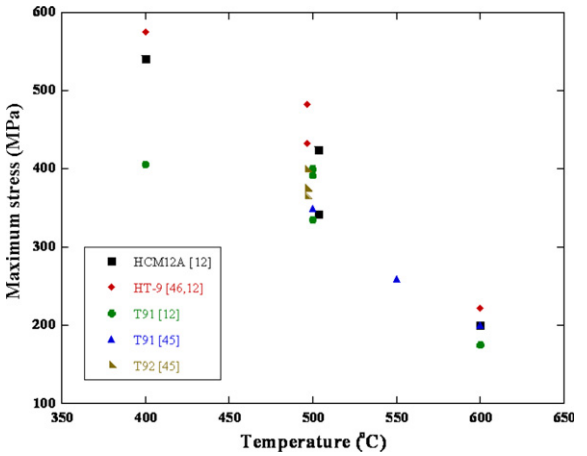


Fig. 42. Maximum stress vs. temperature for ferritic–martensitic alloys. Data points at 500 °C are slightly shifted horizontally so that all symbols could be discerned.

The maximum stress and strain to failure is plotted as a function of temperature in Figs. 42 and 43, respectively. Note that the maximum stress decreases and the strain to failure increases with temperature. Such a temperature dependence would not be observed for alloys that exhibit increasing susceptibility to SCC. Hence, the observed dependence of mechanical properties on temperature is not related to the SCC propensity.

Irradiation was also found to enhance the amount of IG cracking in SCW. HT-9 is known to be susceptible to cracking following irradiation and testing in air [53]. Samples of HT-9 were irradiated with protons at either 400 °C or 500 °C to a dose of 7 dpa and tested in CERT mode in 500 °C

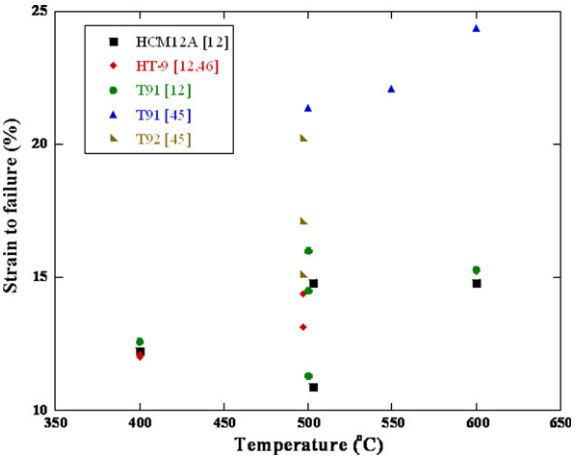


Fig. 43. Strain to failure vs. temperature for ferritic–martensitic alloys. Data points at 500 °C are slightly shifted horizontally so that all symbols could be discerned.

deaerated SCW. Results showed that crack density and crack depth increased due to irradiation and the increase was greatest at 400 °C, Fig. 44. It should be noted that irradiation hardening at 400 °C is quite significant, but is only minimal at 500 °C [54]. Hardening may be controlling the increased susceptibility to IGSCC in HT-9.

One additional set of experiments were performed on grain boundary engineered alloy HT-9 in which the fraction of $\Sigma 1$ grain boundaries was increased by about 30% compared to the as-received (tempered) condition by a deformation and heat treatment process [54]. Fig. 45 shows that both the

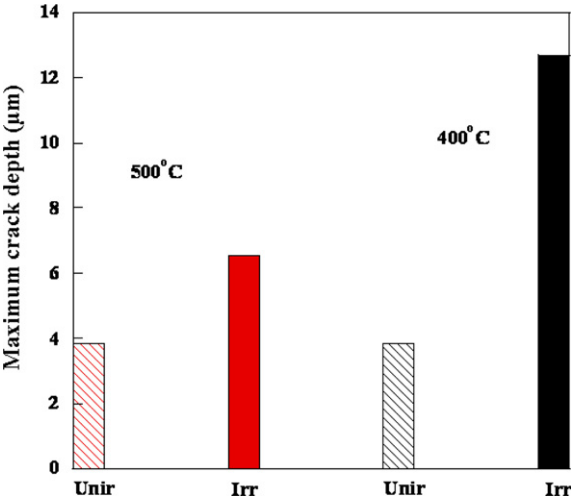


Fig. 44. Effect of irradiation on IG crack depth in HT-9 tested in 500 °C, deaerated supercritical water. The temperatures given in the Figure are the irradiation temperatures [47].

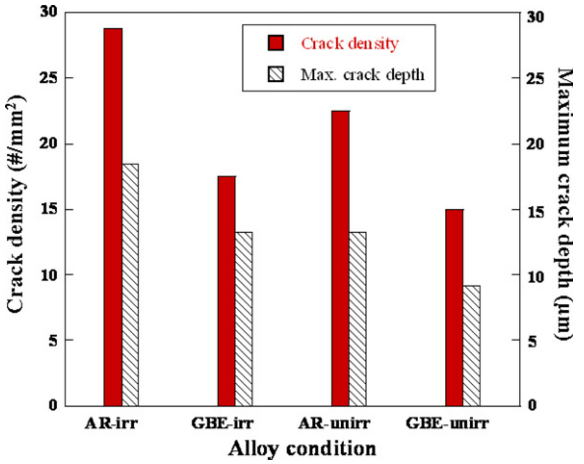


Fig. 45. Crack density and maximum crack depth for HT-9 samples in the as received (AR) condition and in the grain boundary engineered (GBE) condition, and the effect of irradiation on cracking propensity for each condition. Irradiation and CERT testing were both done at 500 °C [54].

crack depth and crack density in the grain boundary engineered samples (GBE) is less than that in the as-received (AR) samples in irradiated at 500 °C and tested in CERT mode in pure, deaerated SCW at 500 °C. The beneficial effect of the GBE treatment is believed to be due to a reduction in the coarsening rate of grain boundary carbides that are believed to be responsible for IG crack initiation.

### 4.4. Other alloys

Very little data exists on Ti alloys in supercritical water, though there is a significant database in subcritical water. The only experiment conducted in SCW was on Ti–15Mo–5Zr–3Al in pure SCW at 550 °C, 25 MPa and 8 ppm dissolved oxygen. The maximum stress was 249 MPa, and the strain to failure was 38%, resulting in a crack density of 26 cracks/mm$^2$ [43]. Similarly, several experiments have been conducted on ODS alloys in subcritical water [25,55], no experiments have been conducted to date in SCW.

### 4.5. Summary of SCC in SCW

The following trends were observed in the stress corrosion cracking behavior in supercritical water.

1. Austenitic stainless steels and nickel-base alloys exhibit greater susceptibility for IGSCC than do the ferritic–martensitic alloys.
2. IGSCC susceptibility, as measured by %IG on the fracture surface decreases with temperature, but as measured by the extent of cracking on the gage section, it increases with temperature.
3. Small additions of HCl or $H_2SO_4$ increase the susceptibility to IGSCC in the austenitic alloys.
4. Increasing system pressure caused an increase in the severity of IGSCC in sensitized 316L stainless steel in pure water with 8 ppm dissolved oxygen.
5. There appears to be an effect of alloy chromium content on SCC cracking propensity in dilute HCl solutions with higher Cr alloys showing greater resistance to IGSCC.
6. With the exception of HT-9, F–M alloys are resistant to IGSCC in pure supercritical water up to 600 °C.

## References

[1] A Technology Roadmap for Generation IV Nuclear Energy Systems, Report No. GIF002-00, 1 December, 2002 (<http://nuclear.gov>).
[2] Feasibility Study of Supercritical Light Water Cooled Reactors for Electric Power Production, Final Report, DE-FG07-02SF22533, INEEL/EXT-04-02539, January, 2005.
[3] P. Kritzer, in: SCR-2000, 6–8 November, 2000, Tokyo.
[4] R. Viswanathan, in: Proceedings of 2000 International Joint Power Generation Conference, Miami Beach, Florida, 2000.
[5] K. Johnston, C. Haynes, Am. Inst. Chem. Eng. J. 33 (1987) 2017.
[6] J. Buongiorno, Massachusetts Institute of Technology, personal communication, June 2005.
[7] R. Viswanathan, R. Purgert, U. Rao, in: Challenges for High Temperature Alloys for Aerospace, Land-Based Gas Turbines, Power and Transportation Symposium, Session 2, High Temperature Alloys in Power Generation, ASM Materials Solutions Conference, Columbus, OH, 18–21 October, 2004.
[8] D.M. Bartels, IWO M2SF02-0060, NERI Quarterly Progress Report, Argonne National Laboratory, 31 January, 2005.
[9] G.S. Was, P.M. Andresen, Chapter in ASM Handbook, Volume 13, Corrosion, American Society for Metals, in preparation.
[10] G.S. Was, P. Andresen, JOM 44 (4) (1992) 8.
[11] G.S. Was, T.R. Allen, in: Proceedings of ICAPP '05, Seoul, Korea, Paper 5690, May 2005.
[12] P. Ampornrat, C.B. Bahn, G.S. Was, in: Proceedings of 12th International Conference on Environmental Degradation of Materials in Nuclear Power Systems – Water Reactors, The Minerals, Materials and Metals Society, 2005, p. 1387.
[13] S. Kasahara, GENES4/ANP2003, paper 1132, Kyoto, Japan, September, 2003.
[14] Y. Tsuchiya, F. Kano, N. Saito, A. Shioiri, S. Kasahara, K. Moriya, H. Takahashi, GENES4/ANP2003, paper 1096, September, Kyoto, Japan, 2003.
[15] J. Jang et al., in: Proceedings of ICAPP'05, Seoul, Korea, Paper 5136, May, 2005.

[16] H.S. Cho, A. Kimura, S. Ukai, M. Fujiwara, J. Nucl. Mater. 329&330 (2004) 387.
[17] T.R. Allen, L. Tan, Y. Chen, K. Sridharan, M.T. Machut, J. Gan, G. Gupta, G.S. Was, S. Ukai, in: Proceedings of Global 2005, Paper IL001.
[18] T.R. Allen, L. Tan, Y. Chen, X. Ren, K. Sridharan, G.S. Was, G. Gupta, P. Ampornrat, in: Proceedings of Global 2005, Paper 419.
[19] T.R. Allen, Y. Chen, L. Tan, X. Ren, K. Sridharan, in: Todd R. Allen, Peter J. King, Lawrence Nelson (Eds.), 12th Environmental Degradation Conference of Materials in Nuclear Power Systems – Water Reactors, TMS, 2006, p. 1397.
[20] L. Tan, Y. Yang, T.R. Allen, Corrosion Sci., in press.
[21] S.A. Bradford, in: Metals Handbook, Ninth Ed.Corrosion, vol. 13, ASM International, Metals Park, OH, 1987, p. 68.
[22] M.J. Graham, R.J. Hussey, Transport in growing oxide films, in: M.A. Dayananda, S.J. Rothman, W.E. King (Eds.), Oxidation of Metals and Associated Mass Transport, The Metallurgical Society, Inc., Warrendale, PA, 1987, p. 85.
[23] Barry Dooley, B. Larkin, L. Webb, F. Pocock, A. Bursik, in: IWC-92-16, Proceeding of 53rd International Water Conference, Pittsburgh, Pennsylvania, October, 1992, p. 154.
[24] B. Dooley, J. Mathews, R. Pate, J. Taylor, Ultrapure Water (1995) 48.
[25] A. Kimura et al., in: Proc. ICAPP'05, Seoul, Korea, Paper 5338, May, 2005.
[26] Y. Chen, K. Sridharan,S. Ukai, T. Allen, J. Nucl. Mater., submitted for publication.
[27] X. Ren, K. Sridharan, T.R. Allen, J. Nucl. Mater., submitted for publication.
[28] J. Kaneda, S. Kashara, in: Proceedings of 12th International Conference on Environmental Degradation of Materials in Nuclear Power Systems – Water Reactors, The Minerals, Materials and Metals Society, 2005.
[29] H. Abe, Y. Watanabe, K. Sue, in: Proc. ICAPP'04, paper 4226, June 2004, Pittsburgh, PA USA.
[30] R. Fujisawa, submitted for publication.
[31] L. Tan, K. Sridharan, T.R. Allen, J. Nucl. Mater. 348 (2006) 263.
[32] Y. Watanabe, H. Abe, Y. Diago, T. Nishida, Corrosion 2004, NACE International, New Orleans, TX, Paper 04493, 2004.
[33] J.H. Jeong et al., in: Proceedings of 12th International Conference on Environmental Degradation of Materials in Nuclear Power Systems – Water Reactors, The Minerals, Materials and Metals Society, 2005.
[34] K. Sridharan, A. Zillmer, J.R. Licht, T.R. Allen, M.H. Anderson, L. Tan, in: Proceedings of ICAPP 04, Pittsburgh, PA, 2004, Paper 4136, p. 537.
[35] A. Motta, A. Yilmazbayhan, M. Silva, R.J. Comstock, G. Was, E. Gartner, Q. Peng, Y. Hwan J., Jeong Y. Park, J. Nucl. Mater., submitted for publication.
[36] S. Teysseyre, Z. Jiao, G.S. Was, Corrosion, in press.
[37] R. Fujisawa, K. Nishimura, T. Kishida, M. Sakaihara, Y. Kurata, Y. Watanabe, Corrosion 2005, NACE International, Houston, TX, Paper 05395, 2005.
[38] C. Bosch, D. Delafosse, Corrosion 2005, NACE International, Houston, TX, Paper 05396, 2005.
[39] G.S. Was, S. Teysseyre, in: Proc. 12th International Conference on Environmental Degradation of Materials in Nuclear Power Systems – Water Reactors, The Minerals, Materials and Metals Society, Warrendale, PA, 2005, p. 1343.
[40] G.S. Was, S. Teysseyre, J. McKinley, Corrosion 2004, NACE International, Houston, TX, Paper 04492, 2004.
[41] W.K. Boyd, H.A. Pray, Corrosion 13 (1957) 375.
[42] H. Matsui, F. Kano, J. Kaneda, Presented at the Project Management Board meeting for the SCWR Materials and Water Chemistry, Ann Arbor, MI, March, 2006.
[43] S. Kasahara, H. Matsui, F. Kano, N. Saito, M. Ookawa, J. Kaneda, in: Proceedings of Workshop on fueled loop tests for SCWR R&D, OECD/NEA, Paris, March, 2006.
[44] S. Teysseyre, G. Jiao, E.A. West, G. Jiao, J. Nucl. Mater., submitted for publication.
[45] L. Fournier, D. Delafosse, C. Bosch, Th. Magnin, in: NACE International Annual Conference, Corrosion 2001, Houston, TX, Paper 01361, 2001, p. 1.
[46] J. Jang, Presented at the Project Management Board meeting for the SCWR Materials and Water Chemistry, Ann Arbor, MI, March, 2006.
[47] G. Gupta, Gary S. Was, in: Proceedings of 12th International Conference on Environmental Degradation of Materials in Nuclear Power Systems – Water Reactors, The Minerals, Materials and Metals Society, Warrendale, PA, 2005, p. 1359.
[48] P. Ampornrat, G.S. Was, J. Nucl. Mater., submitted for publication.
[49] G. Santarini, Corrosion 45 (1989) 389.
[50] G.S. Was, S. Teysseyre, J. McKinley, Z. Jiao, Corrosion 2005, Paper No. 5397, NACE Houston, TX, 2005.
[51] P.M. Scott, in: S. Bruemmer, P. Ford, G.S. Was (Eds.), Ninth International Symposium on Environmental Degradation of Materials in Nuclear Power Systems – Water Reactors, The Minerals, Metals and Materials Society, Warrendale, PA, 1999, p. 3.
[52] R.H. Bricknell, D.A. Woodford, Scr. Metall. 16 (1982).
[53] A. Alamo, X. Averty, Progress Report UT-SM & C-LAM2, CEA report, NT SRMA 99-2316, April 1999.
[54] G. Gupta and G.S. Was, J. Nucl. Mater., submitted for publication.
[55] H.S. Cho et al., J. Nucl. Mater. 329–333 (2004) 387.
[56] J. Kaneda, et al., in: Proceedings of ICAPP'05, Seoul, Korea, Paper 5594, May, 2005.
[57] W. Zielinsky, K.J. Kurzylowski, Scripta Mat. 43 (2000) 33.
[58] D. Briggs, M.P. Seah, in: Practical Surface AnalysisAuger and X-ray Photoelectron Spectroscopy, vol. 1, Wiley, New York, 1990, p. 509.
[59] M. Da Cunha Belo et al., Corrosion Sci. 40 (2/3) (1998) 447.
[60] Y. Chen, K. Sridharan, T.R. Allen, Corrosion 2005, Paper 05391, NACE International, Houston, TX, 2005.
[61] X. Ren, K. Sridharan, T.R. Allen, Corrosion, submitted for publication.